Particle simulation study on the formation of the detached plasma

PIANPANIT, Theerasarn

DOCTOR OF PHILOSOPHY

Department of Fusion Science

School of Physical Sciences
SOKENDAI (The Graduate University for Advanced Studies)

2017 School Year

Abstract

In this work, Particle-in-Cell (PIC) simulation with atomic processes and Coulomb collision has been developed to study the formation of the detached plasma. The Coulomb collision is treated by the binary collision model. The atomic processes that include in our work are the charge exchange, ionization, and excitation. They are treated by the null collision method. The constant input power is introduced in our system. The upstream density is fixed by varying the particle injection inside the source region. The plasma is bounded by particle absorbing and potential floating targets. The uniform neutral gas density region in front of the target is inserted with fixed temperature and pressure.

The transition from the attached to detached plasma when the neutral gas pressure increases is observed. We found the strong reduction of the heat flux when the neutral gas pressure increases. Most of the heat flux is lost via the charge exchange process. The significant reduction of particle flux was not found because the recombination model was neglected in this work. In the case of high neutral gas pressure, after reaching the steady state, the strong temperature gradient profile along the field line inside the neutral gas box is found. The plasma temperature near the target is almost constant and this gives rise to the strong peak of neutral density near the target. The mechanism of this process is caused by the constant particle flux along the field line. When temperature near the target is almost constant, the constant particle flux to the target is sustained by a positive slope in the plasma density because of the proportional of particle flux to the pressure gradient. The time evolution of plasma density profile exhibits the shifting of the neutral density peak from the ionization region to downstream during the detached state. The detached plasma formation is confirmed by the strong total pressure dropping inside the neutral gas region. The sheath structure is self-consistently formed in front of the target, and this structure must be simulated by the fully

PIC simulation. The kinetic effect on the electron and ion distribution functions is observed at the target. In low neutral pressure case, the electron distribution function shows the departure from Maxwellian due to the energetic electron from the upstream plasma. The ion distribution function becomes narrow with the supersonic flow due to the acceleration of ion through the sheath. However, in high neutral gas pressure case, the deviation from the Maxwellian becomes small and it is suggested that in the strong detached state the plasma behavior will approach to fluid model. Also, the shift of the ionization front from downstream to upstream is observed with the strong reduction of the heat flux at the target when the neutral gas pressure increases.

The comparison between the high collisionality and low collisionality is carried out. In low collisionality case, only strong ion temperature gradient is observed and electron temperature does not strongly decrease. The reduction of ionization flux is not observed and also the heat flux does not decrease. These results are explained by the energy loss for each type of atomic processes [Ezumi *et al*, J. Nucl. Mater. **241-243**, 349 (1997)] where the electrons below 5 eV rarely lose their energy through ionization and excitation process. However, if the strong e-i energy relaxation process is triggered as in the high collisionality case, electron energy is transferred to ion and lost their energy to other atomic processes such as the charge exchange.

Contents

Chapter 1

Introduction

1.1 Overview

The edge region where the plasma is colder, contains multiple species and impurities, and is subject to interactions with the vessel-wall materials plays an important role in the the performance of the future fusion reactors. Inside the fusion devices, plasma is confined inside the core by the closed and nested magnetic flux surfaces and heated up to a hundred million kelvins. The plasma remains confined for a finite period of time and it will eventually leave the core region across the last closed flux surface (LCFS) and interacts with the vessel-wall. Inside the tokamak, the external poloidal coil has been used to create the open magnetic field line so that the plasma flows rapidly the to the divertor target before reaching the vessel-wall. The open magnetic field line region is called the scrape-off-layer (SOL) and the power from the core is transported along the SOL to the target. In present devices, the parallel heat flux can go beyond 500 MW/m^2 and estimated to be greater than 1000 MW/m^2 for future devices, such as ITER.[1] The strong heat flux causes the erosion of divertor for long time operation of the fusion devices. At the divertor target, this must be reduced below the limit of the material and must not exceed 10 MW/m^2.

Detached plasma is a method of reducing the heat load to the divertor target.[2, 3] During the detached state, the particle and heat fluxes decrease significantly in front of the target. The detached state is achieved when there is a high neutral gas pressure in front of the divertor. Since the neutral particles are not tied to the field lines, they spread the local heat load to much larger area or even be pumped out

of the system. The different atomic processes play a crucial role in this process for the different type of species, e.g. ion and electron. For ions, this high neutral gas pressure increases the ion-neutral collision rate such as elastic and charge exchange collisions and remove energy flux of ions. For electron, the impurity radiation becomes important to reduce the electron temperature to around 10 eV. After that, ionization becomes dominate and reduce the electron temperature to around 5 eV. After the electron temperature becomes below 5 eV, the e-i relaxation process is the key to reduce electron temperature below 1 eV and the recombination process is triggered to remove the particle flux before reaching the target.[4]

The linear device experiments have been carried out to study the particle and energy transport of the plasma along the open magnetic field line. By inserting the neutral gas chamber between the plasma source and the target and increase the gas pressure to a few mTorr, the results show the strong decrease in the heat load to the target.[5, 6] The detached plasma is clearly observed inside the linear devices. The linear device experiments are done in more comprehensive measurement because of the simple geometry. The first evidence of other atomic processes during the detached state such as molecular activated recombination also has been observed by the linear device experiment.[7] Thus, the results of the linear device are used to study the basic physics of the detached plasma.

The numerical simulation of particle and energy transport of SOL is very important to understand the mechanism of the detached plasma. However, the existence of the non-equilibrium plasma along the SOL due to the boundary of the divertor target causes some theoretical model to have some limitation. The fluid models of collisional transport are based on Maxwellian distribution might be inadequate near the divertor target to predict the energy and particle transport of the high energetic particle tail from the upstream. Many kinetic models has been carried out to investigate the kinetic effect inside the SOL.[8, 9, 10, 11] Another type of phenomena that strongly modulates heat and particle transport into the divertor target is the edge-localized-mode (ELM). During the ELM, high energy charged particles are rapidly burst out from the core and directly move to the divertor target. This may cause excessive heat load onto the divertor plate. The kinetic model also shows the kinetic effect on the plasma transport along SOL during this event. [12, 13]

There are still open issues about the sheath formation at divertor target or

other plasma facing component (PFC). The accelerated ion by the sheath may cause the strong sputtering rate of the neutral atom from the plate, resulting in the net erosion of the divertor target. Various works have been carried out to model the plasma wall interaction.[14, 15], however the fully self-consistent of both the pre-sheath and sheath region is important to give better accurate models. The fully kinetic simulation fully resolves the sheath region because of the spatial and time scales are in the order of Debye length and plasma frequency.[16] Many kinetic simulations also show the results of the sheath structure in various conditions.[17, 18, 19]

The particle-in-cell (PIC) [20] is one of the most powerful kinetic models to simulate the kinetic effect inside SOL. The model self-consistently simulates the plasma-wall boundary condition. The Coulomb, the ion-neutral, and electron-neutral collisions are treated via Monte-Carlo model, in which the collision algorithm for Coulomb collision is the solution of the Landau-Fokker-Planck equation and the for electron- and ion-neutral collisions give the solution of the Boltzmann equation.[21]

1.2 Objectives

In our present work, we aim to simulate the scrape-off layer (SOL) plasma by using the Particle-in-cell (PIC) simulation.

The objectives of this research are

1. To investigate the kinetic processes of detached plasma by using the particle simulation and Monte Carlo collision simulation.

2. To investigate the effect of the neutral gas on the detached plasma.

3. To investigate the dynamics of the detached plasma.

4. To investigate the collision processes that cause the detached plasma near the divertor region.

1.3 Procedure and outline

In this work, the particle-in-cell (PIC) code with the self-consistent electric field has been developed to study the collisional transport of the plasma along the open magnetic field region. The Coulomb collision is treated by using the binary collision model. The plasma-neutral interaction is included via the elastic collision, ion charge exchange, electron impact ionization and electron impact excitation. The model assumes one spatial coordinate along the field line in the x direction and three velocity components (v_x, v_y, v_z).

In this dissertation, the following contents are presented. In chapter 2, the background knowledge of SOL is described. The basic fluid model for the collisional transport and the importance of the kinetic effect on the collisional transport are summarised. The definition of the detached plasma and the overview about the detached plasma can be found. In chapter 3, the simulation model is presented. The details of PIC simulation and the concept of the super particle are explained. The Null collision method for the MCC model and the binary collision method for the Coulomb collision are shown. The details about the parallel computing for PIC simulation are also described. For chapter 4, the simulation parameters and overview of simulation results are presented. The simulation results of the detached plasma are shown in chapter 5, which focuses on the effect of the neutral gas on the detached plasma. Furthermore, the results of the Coulomb collision on the detached plasma are given in chapter 6. The conclusions and discussion follow in chapter 7.

Chapter 2

SOL and plasma detachment

2.1 Scrape-off layer (SOL)

In a magnetic confined fusion device, the behavior and properties of plasma can be affected by the contact with solid surfaces. If the charged particles strike a solid surface it tends to remain and accumulate on the solid surface, thus the solid surface is the plasma sink. The charged particles on the solid surface also recombine and they are released as neutral particles. These neutral particles travel back to the plasma and reionize. If the plasma charged pairs are lost to the surface at the same rate as the recombine neutral particles travel back to the plasma, this is defined as the recycling process as shown in Fig. 2.1.

Let consider a low-pressure gas discharge tube that contains ionized gas. For the first case in which magnetic field has not been applied, the particles move

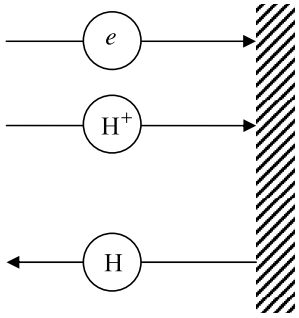

Figure 2.1: When a charged particle that adsorb to the solid surface recombine to neutral particle, it becomes weakly bound to the surface and release back to the plasma. This is particle recycling process.

radially to the wall and interact with the wall as shown in Fig. 2.2 (a). If the magnetic field is applied to the tube as shown in Fig 2.2 (b), the charged particles tend to follow the field line and the radial transport to the wall is reduced. In this case, if the strong magnetic field is applied, a number of particles that fall to the wall decreases, the plasma becomes magnetically confined. For the third case as shown in Fig. 2.2 (c), two circular limiters are inserted inside the tube with inner radius a. Let consider that the particles have very high thermal speed moving along $\mathbf{B}$ but also slowly diffuse along the radial direction. If the particles start to move from the axial of the tube, the particles tend to hit these rings first rather than hit the wall because of the parallel motion is faster than the radial motion. Dense plasma tends to be limited inside the radius a. The less dense plasma that goes beyond the radius a is called the 'scrape-off layer' (SOL).

Now the wall is protected from the plasma because the plasma is concentrated on the limiter. The region that plasma contact with the limiter is called plasma wetted area. The plasma causes the erosion on the target and the eroded material enters the plasma. These impurities degrade the plasma desired properties.

In recent tokamaks, the divertor concept has been proposed for reducing the damage of the first wall from the plasma instead of the limiter. The poloidal magnetic field is generated by plasma current, I_P. The poloidal divertor system is produced by the external current, I_D, as in Fig. 2.3. The poloidal field created by I_P is diverted by the field created by I_D.

Since the magnetic field line makes a figure of eight-shape in the poloidal plane, at some point between the divertor and main plasma becomes null in the poloidal field. This point is called X-point. The field line that passes through the X-point is called separatrix. The separatrix is also defined as the last closed flux surface of the main plasma. Plasma that diffuses across the separatrix is formed at the scrape-off layer (SOL). In the SOL, field lines connect directly to the divertor plate and particles tend to follow the field line to hit the divertor plate rather than diffuse radially to the first wall. Thus the main purpose of the divertor is the same as the limiter, which is to reduce the damage of the plasma to the first wall. Other properties from the divertor, such as to reduce impurity contents, to exhaust the fusion alpha particle, to exhaust the helium ash give the divertor to be a better candidate for the magnetic confinement devices.

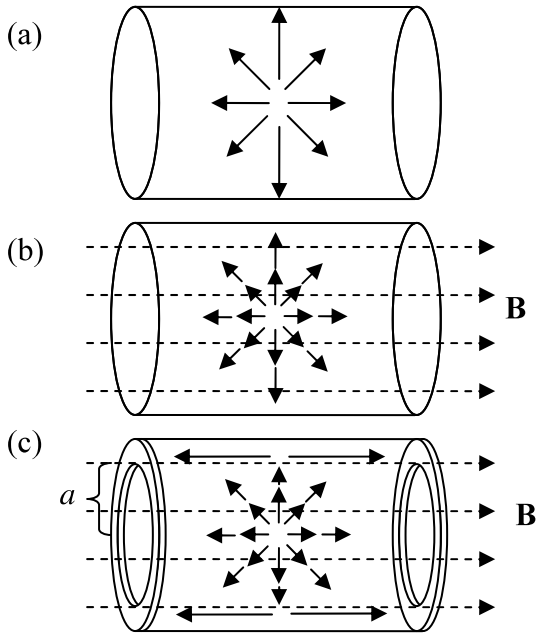

Figure 2.2: Low pressure gas discharge tube. (a) No magnetic field. Plasma move rapidly to the wall. (b) Apply axial magnetic field. Plasma tends to follow the field line but slowly move radially to the wall. (c) With two poloidal ring limiter with inner radius a. At radius a, plasma tend to reach the limiter before reaching the wall.

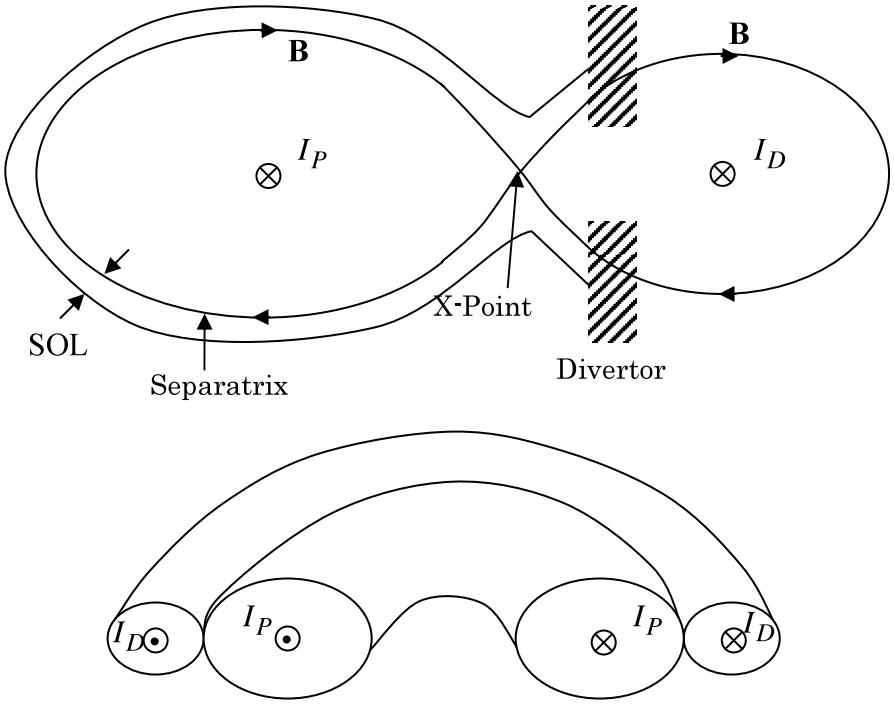

Figure 2.3: Poloidal divertor.

2.2 Kinetic effect of transport in SOL

In the highly collisional limit, the fluid equation of plasma transport along SOL is based on a linear perturbation of the Fokker-Planck kinetic equation[22, 23]. In 1-D case, we assumed the constant magnetic field and the electric field is parallel to the magnetic field line to avoid the appearance of the $E \times B$ drift. Thus, the Fokker-Planck equation is written as

$$\frac{\partial f}{\partial t} + v_x \frac{\partial f}{\partial x} + \frac{qE}{m}\frac{\partial f}{\partial v_x} = \left.\frac{\partial f}{\partial t}\right|_{\text{coll}} + S(x, \mathbf{v}) \tag{2.1}$$

where t is time, x is position parallel to the field line, $\mathbf{v}$ is velocity, E is electric field, $f(x, \mathbf{v}, t)$ is the particle distribution function, $(\partial f/\partial t)_{\text{coll}}$ is the change due to collisions, and S is the rate of particle creation. The fluid equations are obtained by multiplying the kinetic equation with $d\mathbf{v}$, $mv_x d\mathbf{v}$, and $mv^2 d\mathbf{v}/2$ and integrating over the velocity space. The results give the zeroth, first and second moment of the fluid equation with the average values of the velocity distribution which are the density n_s, velocity u_s and temperature T_s where the subscript s represents the species.

However, the two species of plasma can be treated as single fluid equation with plasma density n, velocity u and temperature T by assuming that $n_e = n_i = n$, $u_e = u_i = u$ and $T_e = T_i = T$. The 1-D single fluid equations can be written by

$$\frac{\partial n}{\partial t} + \frac{\partial (nu)}{\partial x} = s_n, \qquad \text{(continuity)} \tag{2.2}$$

$$\frac{\partial (mnu)}{\partial t} + \frac{\partial (mnu^2 + P)}{\partial x} = s_v, \qquad \text{(momentum)} \tag{2.3}$$

$$\frac{\partial}{\partial t}\left(3nT + \frac{1}{2}mnu^2\right) + \frac{\partial}{\partial x}\left(5nTu + \frac{1}{2}mnu^3 - \kappa_{\parallel}^{e}\frac{\partial T}{\partial x}\right) = Q, \qquad \text{(energy)} \tag{2.4}$$

$P = 2nT$ is the plasma pressure, $\kappa_{\parallel}^{e}$ is the electron heat conductivity parallel to a magnetic field line where the ion heat conductivity is neglected. s_n, s_v, and Q are the particle, momentum and energy source. These sources include the i-e and i-n collision terms as the momentum and energy source. This model is use to understand the basic physics of simple SOL. [24, 25, 26]

The fluid model is only valid for highly collision plasma, thus to apply a fluid model for the description of the SOL, a specific ordering of scale lengths is nec-

essary. The necessary condition for a fluid model is that the collision means free path is much smaller than the parallel connection length or plasma gradient length. The heat transport coefficient base on the Braginskii model fails even for small value of $\gamma \equiv \lambda/L_T$, where $\lambda \approx 10^{16} T_e/n_e$ (electron temperature T_e in eV and electron density n_e in m^{-3}) is the collision mean free path and L_T is the temperature gradient scale length $L_T \equiv |\partial \ln T/\partial x|$. The heat transport coefficient usually fails for $\gamma > 0.1$. In a typical tokamak, $\gamma \approx 0.02 - 0.1$ but the high energy electron with energy $E > 3T_e$ has the mean free path almost 10 times longer than typical thermal particle thus the value of γ may be exceeded by this high energy electron. To get more accurate model of collisional transport, other fluid models that include additional terms in the expansion of the distribution function can provide the two-fluid equations that are valid from collisional to weakly collisional limits.[27] However, the kinetic treatment is necessary for verifying and improving the model.

Another major problem that needs the kinetic model to resolve is the sheath formation at the boundary. In SOL, the collisional plasma is bounded by absorbing walls. Due to large different between electron and ion mass, the electron is more mobile and arrives at the divertor target before ion. This creates the potential that strongly decreases toward the target and this potential structure is called the sheath. The sheath accelerates the ions and reflects some part of electrons and adjusts itself to bring about an equal ion and electron flux to the wall.

The size of sheath region is a few Debye length and it is very small compare to the scale length of the SOL in the fusion devices. However, the ions that are accelerated by the sheath may be energetic enough to sputter the neutral atom on the target and cause the erosion of the plate. Kinetic model is necessary for predicting the characteristic of the potential drop for various conditions and has been observed in kinetic simulation.[17, 18, 19] The results from the kinetic simulation are used for the more accurate model of the boundary condition for the fluid model.

2.3 Plasma detachment

International Thermonuclear Experimental Reactor (ITER) is the world largest tokamak which will show the result of the self-burning plasma, in which the heating

of the plasma by the energy from the fusion reaction is sufficient to maintain the temperature of plasma without any external energy input. The magnetic configuration of the present design of the ITER causes the thickness of the SOL to becomes very small, resulting in the very intense area of plasma-wetted area. The parallel heat flux of the ITER at the mid-plane is expected to be around 1 GW/m^2.[1] From the design of the present divertor target, the sustainable heat flux need to be around 10 MW/m^2 during the steady state operation to reduce the erosion rate of the target.

A method to remove all the plasma before reaching the target by inserting a neutral gas box with the pressure of a few millitorr was proposed. The ion-neutral collision would reduce the temperature to below 1 eV where the plasma would recombine before reaching the target. Very few particle flux would reach the target and the main plasma becomes almost separate from the target, thus the word plasma detachment has been introduced for this state. The better definition for the plasma detachment is the state in which the large total pressure drop is observed along the SOL with the strong reduction of the heat and particle fluxes reaching the target.[2]

The above concept was first carried out in a device called quiet energetic dense (QED) device,[6] which is a type of the linear divertor simulator or linear devices. It showed the results of stable detached plasma by puffing gas in front of the divertor target. The results showed the strong decrease in the axial heat flux and the small rise in radial heat flux as the neutral pressure increase. This means that the local heat flux spreads throughout the chamber. The dominant process for energy and momentum removal was the ion-neutral collisions. At high neutral gas pressure, the electron temperature went below 0.2 eV and plasma starts to recombine.

The experiment results from ASDEX [28] showed the relation between the line average plasma density $\bar{n}_e$ and the plasma density at the target n_t. The n_t saturates and starts to fall when $\bar{n}_e$ was increased. At that time the concept of the detached regime was not fully understood until the early 1990s, the detached regimes were observed on most of the divertor tokamak experiment. The ion saturation current measured by the Langmuir probe on the divertor target largely decreases without any decrease in H_α emission during the detached regime.[2, 29, 30, 31] The decrease in ion saturation current corresponds to the decrease in

n_t during the detached regime. The detached regime usually requires the dense plasma of the SOL and it is the regime that follows the high recycling regime of the tokamak, in which the high plasma flux to the target gives rise to the strong recycling rate. The atomic processes play an important role during the detached regime as shown in Fig. 2.4. In this regime with low temperature plasma, the impurity radiation mainly occurs at the electron temperature $T_e \sim$ 10 eV and higher, hydrogen ionization occurs around $T_e \sim 5$ eV and the plasma recombination near $T_e \sim 1$ eV.[4, 5, 6]

Many simulations have been carried out by using the fluid model with the neutral transport code for the simulation of the detached plasma.[32] However, the results of the kinetic effect on the detached plasma have been observed. [10] The energetic electrons from the upstream region deviate the electron distribution function at the target for energy $E > 3T_e$. Other effects such as the sheath and pre-sheath structure during the detached regime also need the fully kinetic simulation to resolve.

Several kinetic model has been carried out to investigate some basic physics of the detached plasma. W1 PIC code was used to investigate the effects of neutrals on the detached plasma.[10] However, only the case of reduced mass ratio was studied. The temporal scale was larger than the plasma frequency, thus the sheath structure was not self-consistently form and was assumed with the ambipolar flow of plasma through the sheath. The PARASOL code self-consistently simulate the sheath, however the atomic processes was treated by simplified model without using the real interaction with neutral particles.[33, 34] The BIT1 code resolves all the above issues but only the high recycling regime related to JET tokamaks study was carried out.[35, 36]

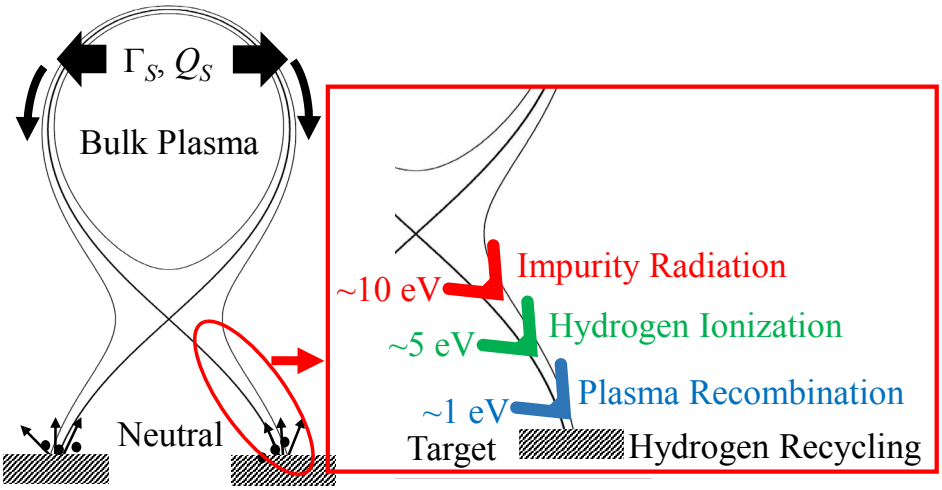

Figure 2.4: Divertor configuration and the atomic processes along the divertor leg.

Chapter 3

Numerical simulations

3.1 PIC simulation

Particle in cell (PIC) simulation[20, 37] has been developed based on the idea of following the motion of each individual charged particle to simulate the behavior of collisionless plasma. Even though the number of particle in the real plasma is much higher than the number of the memory of any computer in the world, the concept of super particle has been introduced so that the statistical properties of the plasma is satisfied without using too many particles.

PIC simulation tracks the trajectory of a collection of the particle by solving a set of differential equations. The particles are tracked along the continuous phase space whereas the field quantities will be calculated in fixed grid point space. PIC simulation can show dynamical kinetic behaviors of the plasma, which are spatial and velocity space distributions of charged particles, self-consistent potential structure. These behaviors help in understanding the physics of plasma.

3.1.1 Basic equations

In PIC simulation, the basic equations for the dynamics of the plasma consist of Newton equation of motion for particle and the Poisson equation for the electric field. The equations of motion are written as

$$\frac{d\mathbf{v}}{dt} = \frac{q}{m}\left(\mathbf{E} + \mathbf{v} \times \mathbf{B}\right), \tag{3.1}$$

$$\frac{d\mathbf{x}}{dt} = \mathbf{v}, \tag{3.2}$$

where $\mathbf{x}$ is particle position, $\mathbf{v}$ is particle velocity, q is the particle charge, m is the particle mass, $\mathbf{E}$ is the electric field and $\mathbf{B}$ is the magnetic field.

The field equations to be solved are

$$\mathbf{E} = -\nabla\phi, \tag{3.3}$$

$$\nabla \cdot \mathbf{E} = \frac{\rho}{\epsilon_0}, \tag{3.4}$$

which are combined to give Poisson's equation as

$$\nabla^2\phi = -\frac{\rho}{\epsilon_0}, \tag{3.5}$$

where ϕ is the electric potential and ρ is the charge density. For $\mathbf{B}$ in our present work is assumed to be time-independent, thus we consider only the electrostatic condition for our simulation.

By giving the initial condition of position, and velocity of each particle, and charge and mass for different species of particle, then the above equation can be solved directly. In our present work, the system is considered to be in one dimension of space but three dimensions of velocity space (1D-3V) or each particle will be given only (x, v_x, v_y, v_z).

3.1.2 Integration of equations of motion and particle weighting

The explicit Boris scheme [20] is used to solve these differential equations. The center-difference for the Newton equation of motion becomes

$$\frac{\mathbf{v}(t+\Delta t/2) - \mathbf{v}(t-\Delta t/2)}{\Delta t} = \frac{q}{m}\left[\mathbf{E} + \frac{\mathbf{v}(t+\Delta t/2) + \mathbf{v}(t-\Delta t/2)}{2} \times \mathbf{B}\right]. \tag{3.6}$$

The Boris scheme separates the electric and magnetic force completely by giving

$$\begin{aligned} \mathbf{v}(t-\Delta t/2) &= \mathbf{v}^- - \frac{q\mathbf{E}}{m}\frac{\Delta t}{2}, \\ \mathbf{v}(t+\Delta t/2) &= \mathbf{v}^+ + \frac{q\mathbf{E}}{m}\frac{\Delta t}{2}. \end{aligned} \tag{3.7}$$

Then $\mathbf{E}$ is removed entirely and (3.6) becomes

$$\frac{\mathbf{v}^+ - \mathbf{v}^-}{\Delta t} = \frac{q}{2m}(\mathbf{v}^+ + \mathbf{v}^-) \times \mathbf{B}, \tag{3.8}$$

which describes the rotation of $\mathbf{v}^-$ to $\mathbf{v}^+$ about an axis parallel to $\mathbf{B}$ by an angle θ where

$$\tan\frac{\theta}{2} = -\frac{qB}{m}\frac{\Delta t}{2}. \tag{3.9}$$

When direction of $\mathbf{v}^-$ and $\mathbf{B}$ are given, $\mathbf{v}^+$ can be determined by the geometry projection on the plane perpendicular to $\mathbf{B}$. This gives

$$\begin{aligned} \mathbf{v}' &= \mathbf{v}^- + \mathbf{v}^- \times \mathbf{t}, \\ \mathbf{v}^+ &= \mathbf{v}^- + \mathbf{v}' \times \mathbf{s}, \end{aligned} \tag{3.10}$$

with $\mathbf{t} = q\mathbf{B}\Delta t/2m$ and $\mathbf{s} = 2\mathbf{t}/(1+t^2)$.

Then the particle position can be advanced by

$$\frac{\mathbf{x}(t+\Delta t) - \mathbf{x}(t)}{\Delta t} = \mathbf{v}(t + \Delta t/2). \tag{3.11}$$

This is the finite-difference equation of the leap-frog method.

To solve the Poisson equation, the charge density in each grid point need to be assigned. The weighting function is necessary to evaluate the value of charge density on each grid point, which can be done by applying some form of interpolation of the grid that closes to the particle position. Different types of weighting for the charge density of a particle are shown in Fig. 3.1. The zero-order weighting is also called the nearest grid point weighting. The whole charge density will be assigned to the nearest grid of a particle. The first-order weighting divides the charge density and assigns to the grid point on the left- and right-hand side of a particle by linear interpolation.

In this work, the first-order weighting is used. If q_c is the charge for each particle and x_i is the position of the i^{th} particle. If X_j is the location of the j^{th} grid point, the charge q_j and q_{j+1} assign to the position X_j and X_{j+1} becomes

$$q_j = q_c \frac{X_{j+1} - x_i}{\Delta x} \tag{3.12}$$

$$q_{j+1} = q_c \frac{x_i - X_j}{\Delta x} \tag{3.13}$$

The force from the electric field to a particle at x_i is also weighted in the same manner. The first-order force comes from the linear interpolation. Thus the electric field $\mathbf{E} = (E, 0, 0)$ for a particle at x_i becomes

$$E(x_i) = \left[\frac{X_{j+1} - x_i}{\Delta x}\right] E_j + \left[\frac{x_i - X_j}{\Delta x}\right] E_{j+1}, \tag{3.14}$$

where E_j and E_{j+1} is the electric field at j^{th} and $(j+1)^{\text{th}}$ grid point.

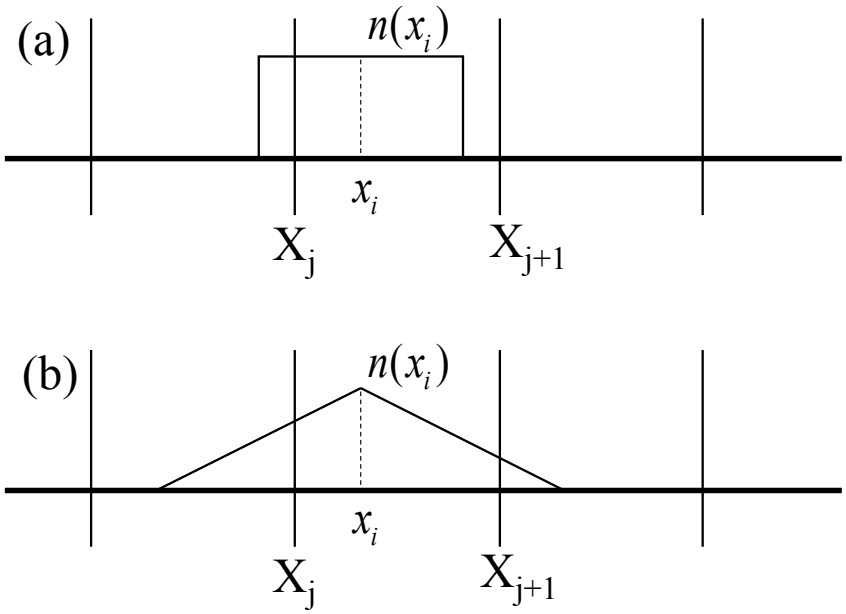

Figure 3.1: The weighting function of particle that locate at x_i for (a) zero-order and (b) first-order.

3.1.3 Integration of field equations and boundary conditions

In SOL the plasma is not spatially periodic. The numerical conditions for 1-D particle simulation for non-periodic with the particle absorption, reflection and emission at the boundary is shown in Ref. 38, 39. Assuming the boundary at both ends of the left- and right-hand side of the system. According to the Gauss' law, the electric field at the boundary becomes,

$$E(L) - E(0) = \frac{1}{\epsilon_0} \int_0^L \rho dx. \tag{3.15}$$

We define the surface charge on the left and right hand side of the boundary as

$$\begin{aligned} \sigma_0 &= \epsilon_0 E(0), \\ \sigma_L &= \epsilon_0 E(L), \end{aligned} \tag{3.16}$$

so that

$$\frac{1}{\epsilon_0} \int_0^L \rho dx + \sigma_0 + \sigma_L = 0, \tag{3.17}$$

and the total charge of the system including the boundaries is zero. This definition depends on the boundary that we want to define. If the boundaries are the con-

ducting wall, then the surface charge will be the actual charge on the walls. If the boundaries are only an end to the system then the surface charges will represent charges beyond the boundary.

By using the finite difference form for the total electrostatic energy in the system and give the condition that the electrostatic energy should be conserved in any choice of the reference potential. This gives the Poisson equation at the boundary as

$$\begin{aligned} \frac{\phi_0 - \phi_1}{\Delta x} &= \frac{1}{\epsilon_0}\left(\sigma_0 + \frac{\rho_0}{2}\Delta x\right), \\ \frac{\phi_N - \phi_{N-1}}{\Delta x} &= \frac{1}{\epsilon_0}\left(\sigma_L + \frac{\rho_N}{2}\Delta x\right), \end{aligned} \tag{3.18}$$

where N is the number of grid in the system. For the potential inside the system, the Poisson's equation in the finite difference form is written as

$$\frac{\phi_{j+1} - 2\phi_j + \phi_{j-1}}{\Delta x^2} = -\frac{\rho_j}{\epsilon_0}, \tag{3.19}$$

where $j = 1, 2, ..., N-1$.

By setting $\phi_N = 0$ for the reference potential, then Eq. 3.19 and boundary conditions can be written in the matrix form as

$$\begin{bmatrix} -1 & 1 & 0 & & & & \\ 1 & -2 & 1 & 0 & & & \\ 0 & 1 & -2 & 1 & & & \\ & & & & \ddots & & \\ & & & 0 & 1 & -2 & 1 \\ & & & & 0 & 1 & -2 \end{bmatrix} \begin{bmatrix} \phi_0 \\ \phi_1 \\ \phi_2 \\ \vdots \\ \phi_{ng-2} \\ \phi_{ng-1} \end{bmatrix} = -\frac{\Delta x}{\epsilon_0} \begin{bmatrix} d_0 \\ d_1 \\ d_2 \\ \vdots \\ d_{N-2} \\ d_{N-1} \end{bmatrix} \tag{3.20}$$

The matrix elements in the right hand side of the equation are

$$d_0 = \frac{\sigma_0}{\Delta x} + \frac{\rho_0}{2}, \;\; d_j = \rho_j, \;\; j = 1, 2, \ldots, N-1 \tag{3.21}$$

In the case of floating potential, where the charge only create inside of the system, σ_0 is calculated from the convection current density at the boundary, J_{conv} by

$$\sigma_0(t) = \sigma_0(t - \Delta t) + J_{\text{conv}}(t)\Delta t \tag{3.22}$$

This current is the current from plasma itself. The verification of the sheath structure by using the planar source model in our PIC simulation is shown in appendix A.

3.1.4 Particle injection

The source function uses in the particle injection model for v_x is from Ref.40. The Emmert source type is written as $S(x,\mathcal{E})d\mathcal{E} = (S_p(x)/2kT_{s0})\exp\{[q\phi(x) - \mathcal{E}]/kT_{s0}\}d\mathcal{E}$ where $S_p(x)$ is injection profile, k is the Boltzmann constant, T_{s0} is the source temperature of specie s, ϕ is the electric potential, and $\mathcal{E}$ is the total energy. Then, writing the right-hand side in terms of $v_x = \sqrt{(2/m)(\mathcal{E} - q\phi(x))}$ the Emmert source type becomes

$$S(x,v_x) = S_p(x)\left(\frac{m\,|v_x|}{2kT_{s0}}\right)\exp\left(\frac{-mv_x^2}{2kT_{s0}}\right). \tag{3.23}$$

For the perpendicular velocity distribution function, the source function is in the Maxwellian distribution function. This type of source function gives the energy flux as $2kT_{s0}\Gamma_{s0}$, where Γ_{s0} is particle flux entering the system. The heat flux by this type of source is the same as one-way heat flux for the Maxwellian distribution function. Thus this type of source gives a Maxwellian distribution function at the mid-plane even with no electric field.[41, 42]

The particle injection model composes of the particle source with the desired injection velocity distribution as $v_x f(v_x)dv_x$. The cumulative flux distribution function is

$$F(v_x) = \frac{\int_0^{v_x} v'_x f(v'_x)dv'_x}{\int_0^{\infty} v'_x f(v'_x)dv'_x}, \tag{3.24}$$

where f is assume to be the Maxwellian distribution function,

$$f(v_x) = A\exp(-v_x^2/2v_t^2), \tag{3.25}$$

where A is the normalization factor, then the cumulative function becomes

$$F(v_x) = 1 - \exp(-v_x^2/2v_t^2) = R \tag{3.26}$$

where R is the random number from 0 to 1. Now the simulation can generate the particle with velocity v_x by the random number R as

$$v_x = v_t\sqrt{-2\ln(1-R)}. \tag{3.27}$$

This function only gives the positive value for the velocity thus we need to assign a random number to define the sign of this Emmert source type.

For the velocity distribution function in y and z direction, a two-dimensional isotropic Maxwell distribution function has been applied. The distribution function can be written as $f(v)dv_ydv_z$ or $f(v)2\pi vdv$ where $v = (v_y^2 + v_z^2)^{1/2}$. The result

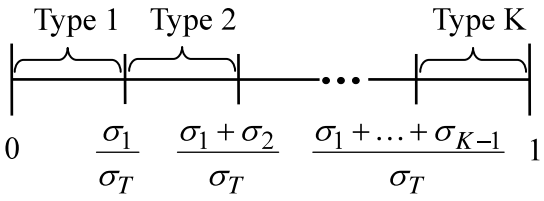

Figure 3.2: Collision probability for selecting the collision type in MCC simulation.

yield the same as the Emmert source type, thus

$$v = v_t\sqrt{-2\ln(1-R)} \tag{3.28}$$

By using another uniform random number R_θ, the value of v_y and v_z then becomes

$$v_y = v_t\sqrt{-2\ln(1-R)}\cos(2\pi R_\theta),$$
$$v_z = v_t\sqrt{-2\ln(1-R)}\sin(2\pi R_\theta).$$

3.2 Monte Carlo collision simulation

In each time step of Monte Carlo collision (MCC) simulation[43], the collision probability of the m^{th} particle is given as

$$P_{\text{collision},m} = 1 - \exp\left[-n_t\sigma_T v\Delta t\right], \tag{3.29}$$

where n_t is the density of target particle, σ_T is the total cross section, v is the relative velocity of collided particles and Δt is the time interval of collision time step. Then the uniform random number R is generated. If $R > P_{\text{collision},m}$ the particle is collided. Another uniform random number is generated to select the collision type by using the cross section of each collision type. The simulation line up the value from σ_1/σ_T, $(\sigma_1+\sigma_2)/\sigma_T$, $(\sigma_1+\sigma_2+\sigma_3)/\sigma_T$, ... , 1 to select the collision type by where the random number fall as in Fig. 3.2. These processes is time consuming, so the alternative way for this simulation are proposed.

In this simulation, the null collision method is used to select the collision type in each time step.[44] In null collision method, the maximum collision probability is calculated instead of calculating every particle collision probability by using the value of maximum collision frequency ν' colliding in a time interval Δt. This value can be written as

$$\nu' = \max_{x,v}(n_t\sigma_T v) = \max_x(n_t)\max_v(\sigma_T v) \tag{3.30}$$

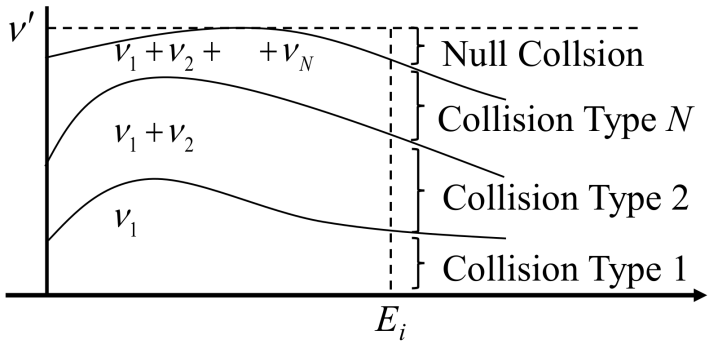

Figure 3.3: Collision probability for null collision method.

Therefore the maximum probability of the particle collision is

$$P_{\text{null}} = 1 - \exp(\nu' \Delta t). \tag{3.31}$$

The number of particles that will be determined the collision type in each time step in a time interval Δt is given by $N_{\text{coll}} = N_P P_{\text{null}}$, where N_P is the number of particles. This process is an advantage of the null collision method because $N_{\text{coll}} \ll N_P$ and only few particles will be selected in each time step. The collision type is selected for each particle, as in Fig. 3.3, where $\nu_i = n_n \sigma_i v$ is the collision frequency for each type of atomic process. The type of collision is determined in the following manner:

$$\begin{aligned}
R &\leq \nu_1(\mathcal{E}_i)/\nu' && \text{(Collision type 1)} \\
\nu_1(\mathcal{E}_i)/\nu' < R &\leq (\nu_1(\mathcal{E}_i) + \nu_2(\mathcal{E}_i))/\nu' && \text{(Collision type 2)} \\
&\vdots \\
(\nu_1(\mathcal{E}_i) + \nu_2(\mathcal{E}_i) + \ldots + \nu_N(\mathcal{E}_i))/\nu' < R & && \text{(No Collision)}
\end{aligned}$$

where R is a uniform random number from 0 to 1. This method needs to be separately treated for each species.

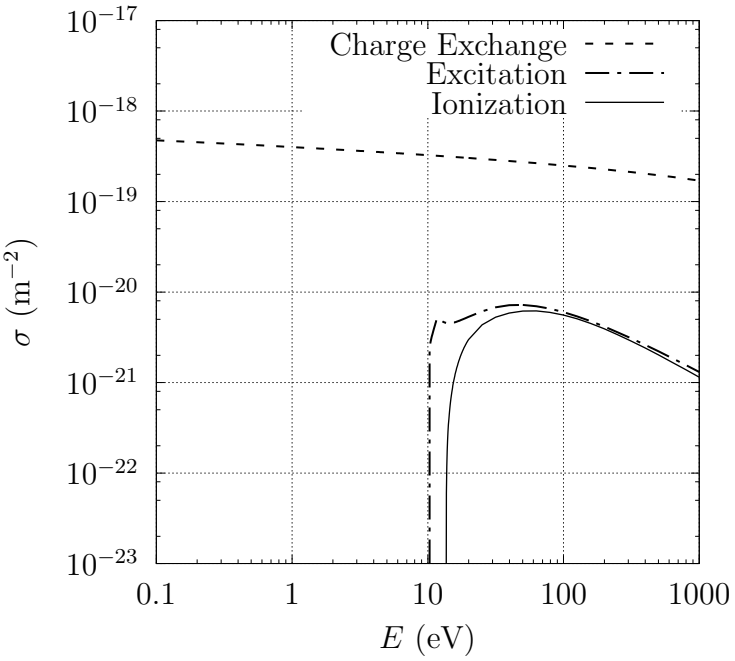

Figure 3.4: The cross section for each atomic processes.

3.3 Collision processes

In the simulation, the atomic processes that have been included are

$e + \mathrm{H}(1s) \rightarrow e + \mathrm{H}(2p)$ (Excitation)

$e + \mathrm{H} \rightarrow e + \mathrm{H}^+ + e$ (Ionization)

$\mathrm{H}^+ + \mathrm{H} \rightarrow \mathrm{H} + \mathrm{H}^+$ (Charge Exchange)

The cross sections of collision processes are shown in Fig. 3.4, in which the excitation, ionization and charge exchange cross section data are from Ref. 45, 46, 47.

These atomic processes of H and H^+ can strongly influence the plasma behaviour at the plasma temperature below 10 eV. The recombination process is omitted in this simulation. The energy threshold for excitation and ionization process are 10.2 and 13.6 eV.

3.3.1 Electron-neutral collisions

In the electron-neutral collision, the large ratio of neutral to electron mass causes the neutral momentum remain approximately the same after the collision. Neutral gas velocity is also very slow compared to electron velocity, thus the relative velocity of neutral gas and electron is approximated as the electron velocity.

Let consider the energy of scattered electron in each process. In the case of electron-neutral elastic collision, the electron is scattered with no energy transfer to the neutral atom.

In the case of electron-neutral excitation collision the energy of the scattered electron is

$$\mathcal{E}_{\text{scatterred}} = \mathcal{E}_{\text{incident}} - \mathcal{E}_{\text{excitation}} \tag{3.32}$$

In the case of electron-neutral ionization collision, the created electron energy need to be considered. Thus the sum of scattered electron energy with created electron energy is equal to incident electron energy minus the ionization energy, or

$$\mathcal{E}_{\text{scatterred},e} + \mathcal{E}_{\text{created},e} = \mathcal{E}_{\text{incident},e} - \mathcal{E}_{\text{ionization}} \tag{3.33}$$

For created ion, the model assumes that the created ion energy and momentum is equal to the incident neutral particle energy and momentum, or

$$\mathcal{E}_{\text{created},i} = \mathcal{E}_{\text{incident},n} \tag{3.34}$$

$$v_{\text{created},i} = v_{\text{incident},n} \tag{3.35}$$

From Eq. 3.33, the scattered electron energy is calculated from the differential ionization cross section[48, 44] and becomes

$$\mathcal{E}_{\text{scatterred},e} = B \tan\left[R \arctan\left(\frac{\mathcal{E}_{\text{incident},e} - \mathcal{E}_{\text{ionization}}}{2B}\right)\right] \tag{3.36}$$

where B is a known parameter ($B = 10$ in present work).

Now consider the direction of the velocity of scattered electron (and created electron). The incident electron scatters as in Fig. 3.5, in which $\hat{\mathbf{v}}$ and $\hat{\mathbf{v}}'$ are unit vectors parallel to the incident and scattered velocities respectively. The angle ϕ, which

$$\phi = 2\pi R \tag{3.37}$$

is uniformly distributed from 0 to 2π. The angle χ can be approximated in the form of differential cross section [49], which is

$$\frac{\sigma(\mathcal{E},\chi)}{\sigma(\mathcal{E})} = \frac{\mathcal{E}}{4\pi\left[1 + \mathcal{E}\sin^2(\chi/2)\right]\ln(1+\mathcal{E})}, \tag{3.38}$$

where $\mathcal{E}$ is the energy of incident electron in eV. The random number R from 0 to 1 is solved from

$$R = \frac{\int_0^{\chi} \sigma(\mathcal{E},\chi')\sin\chi' d\chi'}{\int_0^{\pi} \sigma(\mathcal{E},\chi')\sin\chi' d\chi'}. \tag{3.39}$$

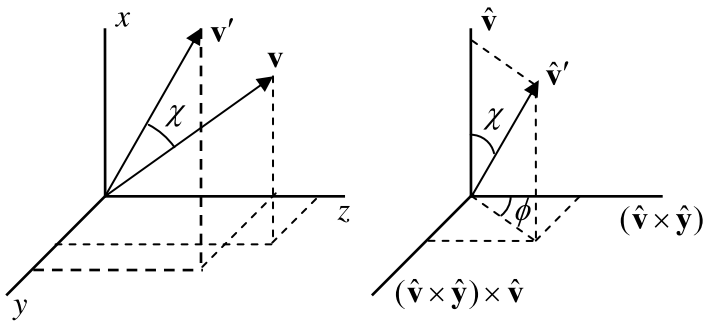

Figure 3.5: Incident particle scattering angle.[50]

Then the scattering angle can be written as

$$\cos\chi = \frac{2+\mathcal{E}-2(1+\mathcal{E})^{R}}{\mathcal{E}}. \tag{3.40}$$

If the incident electron energy is low enough, this function becomes uniformly distributed from -1 to 1 or

$$\cos\chi = 1-2R. \tag{3.41}$$

In Fig. 3.5, $\hat{\mathbf{v}}'$ is written in the form of $\hat{\mathbf{v}}$ by

$$\hat{\mathbf{v}}' = \hat{\mathbf{v}}\cos\chi + (\hat{\mathbf{v}}\times\hat{\mathbf{y}})\sin\chi\cos\phi + [(\hat{\mathbf{v}}\times\hat{\mathbf{y}})\times\hat{\mathbf{v}}]\sin\chi\sin\phi \tag{3.42}$$

3.3.2 Ion-neutral collisions

For ion-neutral collision cases, the assumption that the neutral particle is stationary compared to the incident particle is invalid. So the simulation generates the isotropic Maxwellian distribution velocity for the neutral particle at T_n and finds the ion relative velocity to the neutral particle by subtracting ion velocity with neutral velocity. After the collision, ion velocity is transferred back to its original frame by adding back the subtracted neutral velocity.

In the charge exchange collision, the incident ion only transfers its charge to the neutral particle, thus the ion takes the velocity of the incident neutral particle and the neutral particle takes the velocity of incident ion. This process resembles the 180-degree scattering of the hard sphere model in the elastic collision. This simple approach yields a momentum transfer cross section of about $2\sigma_{\text{ex}}$, where σ_{ex} is the charge exchange cross section. However, this relation only holds for the

plasma temperature greater than 2 eV. At lower energy the small-angle elastic scattering need to be considered.[51]

3.4 Coulomb collision

In the PIC model, the finite size particles have been used to solve the self-consistent electric field. The finite size particle does not change the phenomena with wavelength larger than a cell size. However, it does not accurately treat Coulomb collision and the Coulomb collisions are damped out inside the cell[52, 53], thus the plasma in PIC model is assumed to be collisionless. For the simulation of the low temperature with high density plasma in the SOL regions, the Coulomb collision becomes important and should not be omitted.

The effect of Coulomb collision is often treated by applying the binary collision model between charged particle. Shanny et al. first introduce a one-dimensional electron plasma model, in which the electron collides with the stationary ions and scatter in three-dimensional velocity space by using the Lorentz gas collision model.[54] Takizuka and Abe proposed a better way for the binary collision model by using the Monte Carlo method.[55] In each collision time step the particles are paired and collide within the cell and the scattering angle for changing the velocity of each particle is directly calculated. Rather than calculate the small scattering angles in small collision time step, Nanbu grouped the scattering angle into a large cumulative scattering angle.[56] Base on the Nanbu assumption, Bobylev et al. showed that the Nanbu model is a solution method of the Landau-Fokker-Planck equation.[57] The Nanbu model reduces the computational time of the binary collision and it is also more accurate than the Takizuka and Abe model.[58]

To determine how large is the scattering angle after N collisions of a particle, assume that a test particle starts with relative velocity $\mathbf{g}_0$, after the $1^{\text{st}}, 2^{\text{nd}}, \ldots, \text{N}^{\text{th}}$ collisions, the relative velocities are $\mathbf{g}_1, \mathbf{g}_2, \ldots, \mathbf{g}_N$. Because the Coulomb collision is elastic, the relative speed g must be conserved, thus $g = |\mathbf{g}_1|, |\mathbf{g}_2|, \ldots, |\mathbf{g}_N|$. The cumulative scattering angle χ is defined as the angle between $\mathbf{g}_0$ and $\mathbf{g}_N$ or

$$\cos\chi = \mathbf{g}_0 \cdot \mathbf{g}_N / g^2 \tag{3.43}$$

Nanbu discovered that the expectation value of $\sin^2(\chi/2)$ is

$$\left\langle \sin^2\frac{\chi}{2} \right\rangle = \frac{1}{2}(1 - e^{-s}). \tag{3.44}$$

The parameter s is introduced as the isotropy parameter and expressed as

$$s = n_t g \pi b_0^2 (\ln \Lambda) \Delta t, \tag{3.45}$$

where n_t is the target particle density, and b_0 is the classical distance of the closest approach. The probability of finding $\mathbf{g}_N$ scatter in solid angle $d\Omega$ is $f(\chi)d\Omega$ and by fitting with the expectation value gives

$$f(\chi) = \frac{A}{4\pi \sinh A} \exp(A \cos \chi) \tag{3.46}$$

The constant A is determined by s in the following equation:

$$\coth A - A^{-1} = e^{-s}. \tag{3.47}$$

The above equation needs to be calculated in advance and saved to an array to reduce the computational time. By using this constant A, χ_N is calculated from the following equation:

$$\cos \chi_N = \frac{1}{A} \ln \left(e^{-A} + 2R \sinh A \right), \tag{3.48}$$

where R is the uniform random number and this function gives $-1 < \cos \chi < 1$.

The Nanbu method can be applied for both equally weighted particles and non-equally weighted particle. [59, 21] In our present work, the equally weighted particle was used. In the PIC simulation, the computational domain is divided into small cells in the scale of the Debye length, thus in each cell the binary collision is treated separately. For two-component plasma, the number of particle α colliding with particle β is

$$N'_\alpha = \frac{N_\alpha N_\beta}{N_\alpha + N_\beta}, \tag{3.49}$$

and the remaining number of particle α colliding with particle α are

$$N''_\alpha = N_\alpha - N'_\alpha = \frac{N_\alpha N_\alpha}{N_\alpha + N_\beta}. \tag{3.50}$$

This pairing method is shown in Fig. 3.6. Then the scattering angle of each pair of the particle is calculated. However, if N''_α is odd number, the last 3 particles that will collide will be pair to each other as shown in Fig. 3.6(b) and the time step that is used to calculate the scattering angle will be modified as

$$\Delta t_{\text{coll}} = \frac{N''_\alpha}{N''_\alpha + 1} \Delta t \tag{3.51}$$

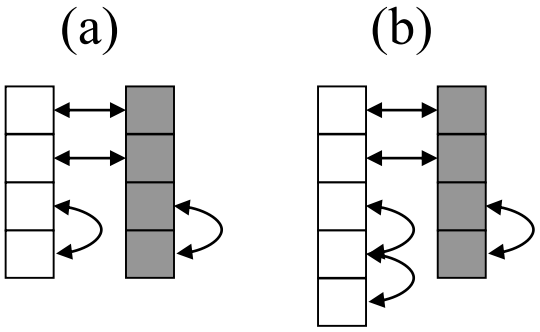

Figure 3.6: The selection of binary collision pair with same and different species for the case of (a) an equal number of the particle between each species and (b) a different number of the particle between each species.

The scattering angle for each pair is calculated using Eq. (3.48) and the new velocity vector is obtained as displayed in Fig. 3.5.

We applied the Nanbu model to the PIC simulation by using the periodic boundary condition. The simulation gave good results of the energy relaxation process of the charged particle and the results are shown in Appendix B.

3.5 Numerical heating

In the PIC simulation, even when the time step and grid size satisfy the stability condition, the numerical heating is still observed. In the 1-D PIC simulation using only one species, it is found that the plasma temperature increases linearly with simulation time.[60, 20] Here, a self-heating time τ_H is defined as the time for the plasma temperature to double. The parameter needs to be carefully selected to avoid the self-heating of the plasma or else the plasma total energy will not be conserved. For the PIC simulation with linear weighting, using $v_t \Delta t/\Delta x \approx 1/2$ gives the self-heating time as

$$\frac{\tau_H}{\Delta t} \approx \frac{600}{\omega_p \Delta t}\left(\frac{\lambda_D}{\Delta x}\right)^2 \left(1+\frac{\lambda_D}{\Delta x}\right) N_C \tag{3.52}$$

where N_C is the number of particle per cell. The PIC simulation results with the periodic boundary condition are shown in Fig. 3.7 by using $\Delta x/\lambda_D = 1/2$ and $\omega_p \Delta t = 1/4$. The heating time is in the order of 10^6 time steps. In the normal PIC simulation, $N_C \approx 200$ and the heating time is only in a few million time step.

From the above equation, to increase the heating time the parameter such as Δx and Δt need to be small and also N_C need to be large enough.

The numerical heating of the PIC simulation mainly causes by the finite size of the superparticle. The spatial smoothing for the electric potential profile is used to suppress the numerical heating for large simulation time. If the electric potential is solved by the Fourier transform, the filtering is done in k-space to reduce noise from the short wavelength. This is easily done by multiplying some filtering factor with $\phi(k)$. But in our work, the potential is solved by direct finite difference method in x space. Thus the filtering must be done in x space and is called the digital filtering. The new smoothing potential is written as

$$\phi'_j = \frac{\phi_{j-1} + 2\phi_j + \phi_{j+1}}{4}. \tag{3.53}$$

If N_{smooth} is the number of time to apply this filtering, the coefficients for $N_{\text{smooth}} =$ 1, 2 and 3 are

$$\begin{aligned}
\phi' &: \frac{1}{4}(1, 2, 1), \\
\phi'' &: \frac{1}{16}(1, 4, 6, 4, 1), \\
\phi''' &: \frac{1}{64}(1, 6, 15, 20, 15, 6, 1).
\end{aligned}$$

If N_{smooth} is large enough, the numerical heating is totally suppressed.

3.6 Parallel PIC-MCC

The workloads for the computation for the PIC-MCC simulation depend mainly on the particle pushing between each cell, the particle interaction between each other and the field solver. The parallel computing is applied to decompose the workload for the computation. The two main strategies often use are the particle decomposition [61, 62, 63] and the domain decomposition[64, 65]. Domain decomposition consists in dividing each spatial grid into different processes along with the particles that locate on that region. Particle decomposition distributes the particle among the processes while giving the whole domain to each process. In general, the particle decomposition is more efficient than the domain decomposition even though the surplus of the memory usage for the field quantities need to be assigned for every process. The domain decomposition reduces the memory

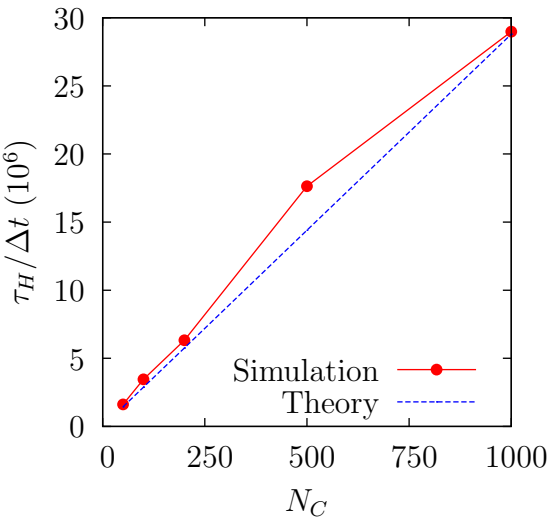

Figure 3.7: The number of time step for the heating time vs. the number of particle per cell for the case of PIC with linear weighting with $\Delta x/\lambda_D = 1/2$ and $\omega_p \Delta t = 1/4$.

usage of the field quantities however it requires the communication between each process for pushing the particle into the different domain and the dynamic load balancing.

In the PIC-MCC, the interaction between particles within the cell is necessary and the domain decomposition is a better option for the parallel computing. The domain is divided into small region depending on the number of particle in each cell. In our work, due to the non-uniform plasma density, the domain size for each process are not equal as shown in Fig. 3.8. We apply the dynamic load balancing, in which the size of the domain changes in a fixed time step the number of particle dividing in each process is shown in Fig. 3.9. The comparison between the number of particles in each node with the average number of particles is less than 1%.

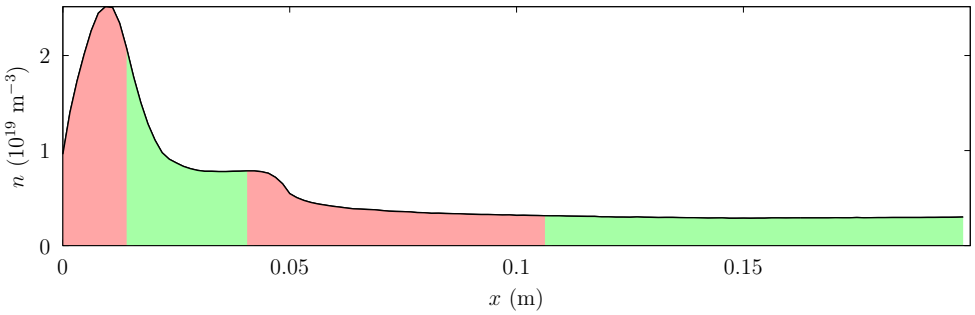

Figure 3.8: The sub-domains are created for 4 node parallel processors for simulations with uniform grid spacing. Sub-domains have nearly equal numbers of particles, but unequal physical size.

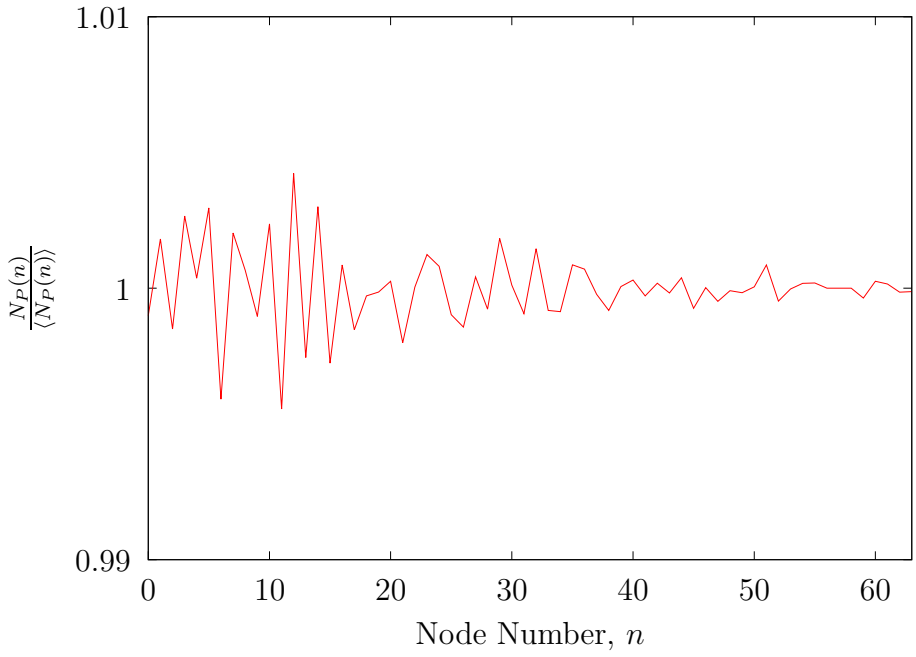

Figure 3.9: The plot between the ratio of number of particle in each node $N_P(n)$ to the average number of particle $\langle N_P(n)\rangle$ with the node number n by using the case of plasma density that shown in Fig. 3.8. The average number of particle is calculated by the total number of particles in the system over the number of node.

Chapter 4

Simulation Results

4.1 Simulation parameters

The system is divided into three regions which are the source region, the source free region, and the neutral gas region as shown in Fig. 4.1. The source region is where the particles are uniformly injected into the system. The neutral gas region is where the plasma interacts with uniformly distributed neutral gas. The distribution function of the neutral gas is assumed to be in Maxwellian with no flow velocity. In the present study, dynamics of neutral gas is not included. Once particles are injected into the system, they flow along magnetic field lines that are oriented parallel to the x-axis. The magnetic field $\mathbf{B} = (B_0, 0, 0)$ is assumed to be constant along the x-axis. Particles that cross the symmetry midplane located at $x = L$ are reflected back to the system. This process conserves the momentum and kinetic energy of the reflected particle. Particles that are incident upon the

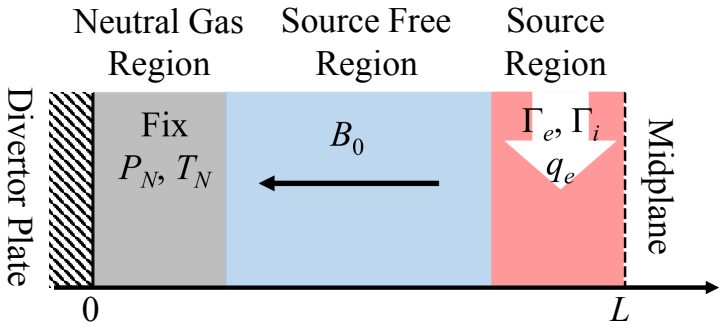

Figure 4.1: System configuration with the plasma source on the right-hand side and the divertor target on the left-hand side.

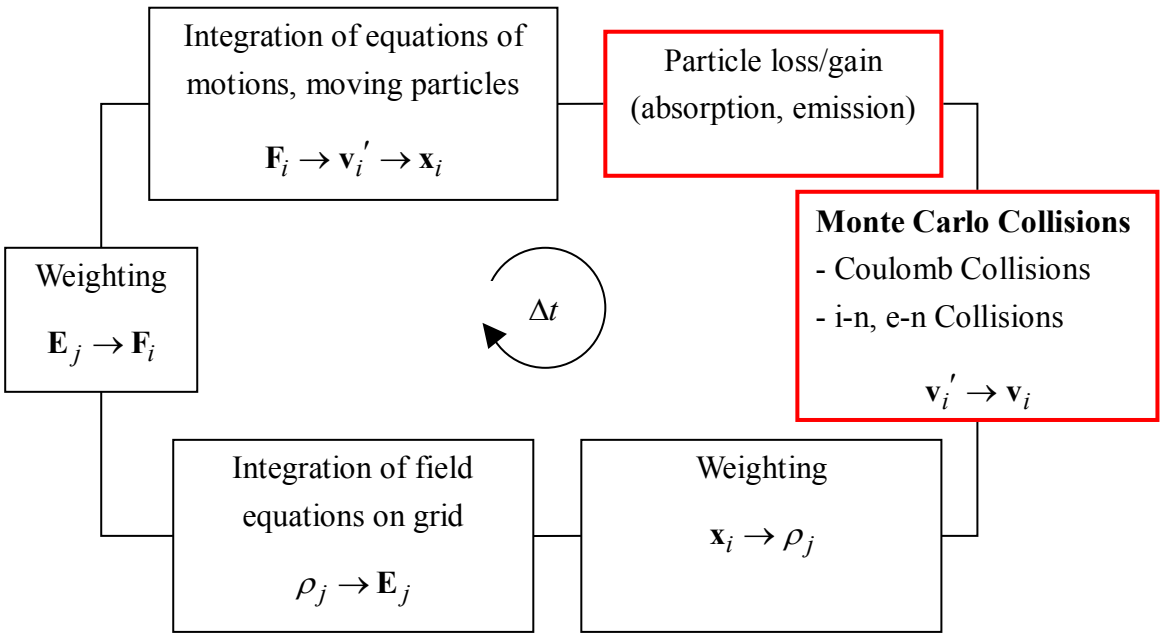

Figure 4.2: A flow chart for one time step in the PIC-MCC code. The red boxes show the additional scheme for the particle loss, gain and MCC model. The particles are labelled with index i and the field quantities are obtained only on the spatial grid with index j.

divertor plate are absorbed on the surface of the plate. Ion and electron reflection, recycling process, and secondary electron emission are not included in this work. The charge of the absorbed particles is added to the net plate surface charge, hence the plate is assigned with floating potential.

The flow chart of the simulation in each time step is shown in Fig. 4.2. First, we calculate the loss and gain of the particle into the system due to the source and sink region. Then the Monte Carlo collision processes are treated. Each particle is weighted to find the charge density and this charge density gives the electric field on the grid points. The electric field is weighted to calculate the force on each particle inside the cell and then the particle accelerates and moves to new location.

The source function used in the particle injection model for v_x is from Emmert et al. [40] and the details of the source function are shown in section 3.1.4. In the present work, electrons and ions are injected with the same particle flux $\Gamma_{e0} = \Gamma_{i0} = \Gamma_0$, where $\Gamma_0 = \Delta N/(\Delta t A)$, ΔN is number of injected particle in each time step and $A = 1$ m^2 is injected area. The particles are injected with a constant

System length	$L = 0.2$ m
Plasma source length	$L_S = 0.05$ m
Neutral source length	$L_N = 0.05$ m
Mass ratio	$m_i/m_e = 1836$
Source temperature	$T_{e0} = T_{i0} = 10$ eV
Super particle size	$N_S = 1 \times 10^{11}$
Neutral gas temperature	$T_N = 0.1$ eV
Neutral gas temperature	$q_{\rm inp} = 0.4$ MW/m^2
Upstream density	$n_u = 3 \times 10^{18}$ m^{-3}
Magnetic field	$B_0 = 1$ T

Table 4.1: Simulation parameters.

rate until the upstream density reaching the fixed value n_u, then the injection rate is decreased until the system reaching the steady state with fixed value of the upstream density. The heating term $q_{h,e}$ is included in the source region so that the total input heat flux becomes constant. For the heating term in our simulation, we randomly choose a particle inside the source region and randomly calculate new energy from the Maxwellian distribution function for that particle. The new velocity is assigned to the particle without changing the direction of the particle velocity. In this work, only electrons are heated so that the distribution function of both electron and ion will maintain the Maxwellian distribution at the mid-plane. Thus the total input heat flux can be expressed by the following terms:

$$q_{\rm inp} = (2kT_{e0} + 2kT_{i0})\Gamma_0 + q_{h,e} \tag{4.1}$$

The simulation parameters are shown in table 4.1. The real hydrogen mass ratio has been used in this simulation thus the flow velocity of the ion is the real value. In the simulation, the collisional acceleration factor $\alpha_{\rm coll}$ is defined as the ratio of the Coulomb collision frequency in the simulation to the real value of the collision frequency and can be written as

$$\alpha_{\rm coll} \equiv \frac{\nu_c^{\rm code}}{\nu_c^{\rm phys}} = \frac{\nu_c^{\rm code}}{\left(\frac{\ln\Lambda}{4\pi}\left(\frac{q_\alpha q_\beta}{\varepsilon_0 \mu_{\alpha\beta}}\right)^2 n v_{Te}^{-3}\right)}, \tag{4.2}$$

where $\mu_{\alpha\beta}$ is the reduced mass of particle species α and β, v_{Te} is electron thermal velocity and $\ln\Lambda$ is the Coulomb logarithm.[42, 9] The isotropy parameter from

Eq. (3.45) in Nanbu model becomes

$$s = n_t g \pi b_0^2 (\ln \Lambda) \alpha_{\rm coll} \Delta t. \tag{4.3}$$

When this factor increases, the scattering angle of each pair of collision becomes larger. Thus time of the energy relaxation between electron and ion decreases. The value of $\alpha_{\rm coll}$ determines the Coulomb collisionality $\nu^* \equiv \nu_{c0}/\nu_{be0}$, where ν_{c0} is the Coulomb collision frequency between ion and electron from the source region and ν_{be0} is the bounce frequency where $\nu_{be0} = v_{te0}/L$ and v_{te0} is the source electron thermal velocity.[8, 42] These give $\nu^* \sim 10^{-16} n_u L/T_{e0}^2$ (T_{e0} in eV, n_u in m^{-3}, and L in m).

4.2 Overview of simulation results

The simulation of the detached plasma in this study is focused on the effect of the neutral gas pressure and the effect of Coulomb collision on the detached plasma. The effect of the neutral pressure is studied by fixing $\alpha_{\rm coll} = 100$ and varying the neutral gas pressure where $0 \leq P_N \leq 20$ mTorr. The effect of Coulomb collision is studied by giving $\alpha_{\rm coll} = 1,\ 10,$ and 100.

At $t = 0$ s, each simulation assumes that no plasma inside the system. The simulation starts with the injection of uniformly distributed electron-ion pairs to the system with constant rate and the rate is reduced to fix the upstream plasma density. The phase space plot of electron and ion are shown in Figs.4.3, which shows the time evolution of the plasma at the initial state. The plasma flows from the source region to the neutral gas region and collides with neutral particles. The simulation runs until reaching the steady state, where the average plasma density of the whole system, $\bar{n}$, saturates as shown in Fig. 4.4. The time to reach the steady state is estimated as $t_{\rm sim} \sim 2L/u_i$, where u_i is the ion flow speed which $u_i\ c_s$ where c_s is the ion acoustic speed. By giving $T_e = T_i = 10$ eV then $t_{\rm sim} \sim 9\ \mu$s and this almost correspond to $P_N = 0$ mTorr case. The strong ion-neutral collision in high neutral gas pressure removes momentum from ion and slow down the ion flow speed. This result causes the simulation time to become longer. The decrease in the ion flow speed also causes the confinement time for the particle inside our system to increase. Thus in high neutral gas pressure, the larger value of $\bar{n}$ is observed.

$\alpha_{\text{coll}} = 1,\ 10$		
P_N (mTorr)	Δt (s)	N_g
0	8×10^{-13}	20,000
5	8×10^{-13}	25,000
10	8×10^{-13}	30,000
15	8×10^{-13}	35,000
20	8×10^{-13}	40,000

Table 4.2: Simulation parameters for the time step size and the number of grid for $\alpha_{\text{coll}} = 1,\ 10$.

The simulation is carried out by setting the time step Δt and the number of grid N_g as shown in table 4.2 and 4.3. Due to the non-uniform plasma density and temperature in our result, the stability condition for the explicit PIC simulation such as $\omega_p \Delta t$ and $\Delta x/\lambda_D$ need to be treated in a careful manner. The spatial profile results of $\omega_p \Delta t$ are shown in Fig. 4.5 where $\omega_p \Delta t < 0.2$ and the parameter for Δt give a good stability condition. The results of $\Delta x/\lambda_D$ are shown in Fig. 4.6 in which almost all regions satisfy the condition for $\Delta x/\lambda_D < 1$.

The numerical heating is tested by using the periodic boundary condition with the plasma density $\bar{n} = 1.5 \times 10^{18}$ and temperature $T_e = T_i = 10$ eV. As mention above the time to reach the steady state can be approximated by $2L/u_i$. We use $\Delta t = 8 \times 10^{-13}$ and $t_{\text{sim}} = 8\ \mu$s (10 million time step). The results show that the total energy of the plasma increases around 10% in the periodic boundary system. This error gives the non-physical result of the total heat flux to the wall by using the PIC simulation. The digital filtering as mention in section 3.5 is applied in each time step by giving $N_{\text{smooth}} = 1$, 5 and 10. The result shows a strong reduction of the numerical heating from 10% to 5%, 0.4% and 0.2%.

In this work, the $N_{\text{smooth}} = 5$ is chosen. The numerical heating is measured by $(\mathcal{E}_{\text{loss}} + \mathcal{E}_{\text{wall}})/\mathcal{E}_{\text{inp}}$, where $\mathcal{E}_{\text{loss}} + \mathcal{E}_{\text{wall}}$ is the sum of the energy loss by the atomic processes with energy loss at the target and $\mathcal{E}_{\text{inp}}$ is the total input energy. The results of this ratio are shown in Fig. 4.7 and all of the results are less than 5%.

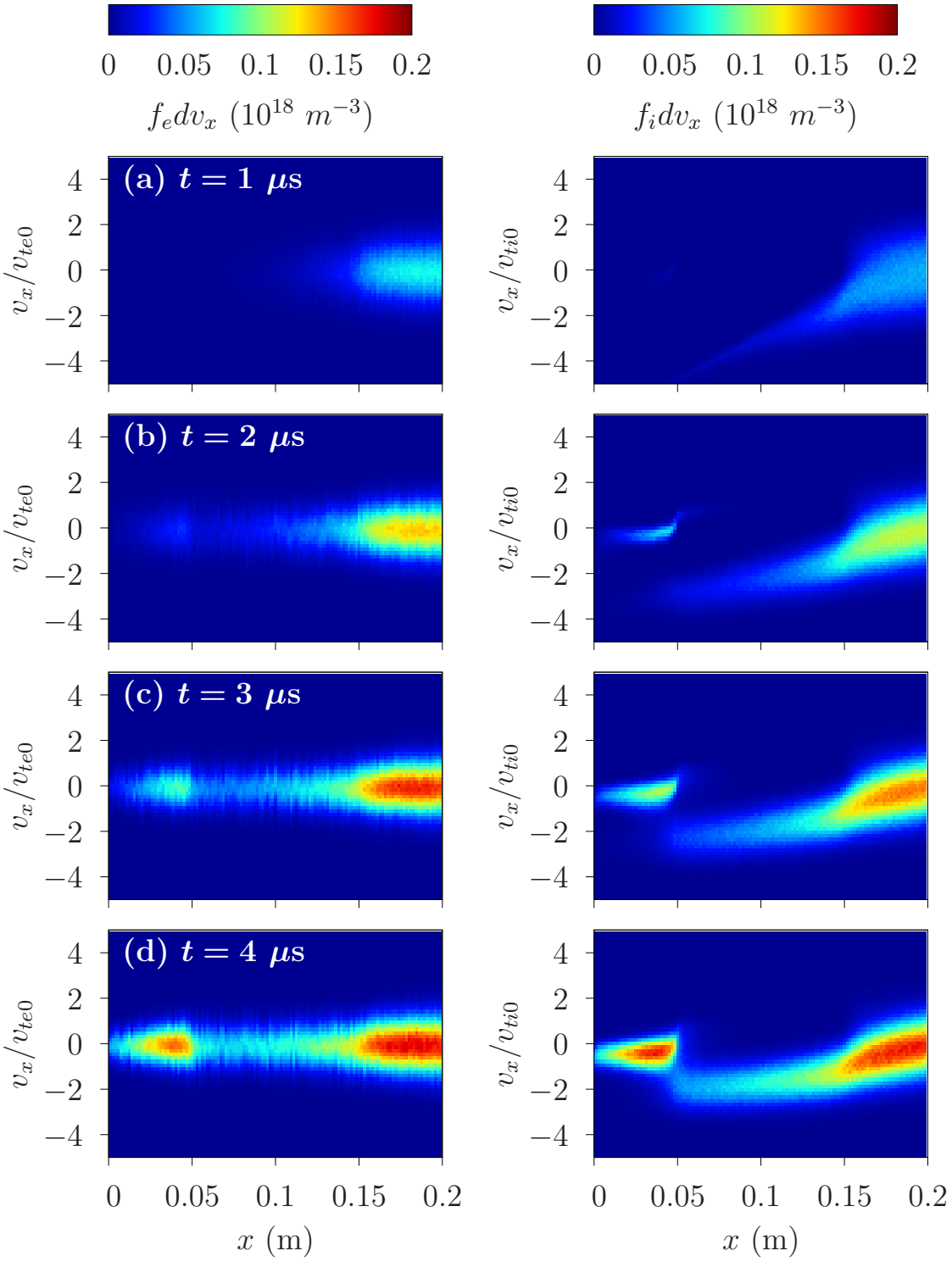

Figure 4.3: Time evolution of the phase space plot of electron (left panel) and ion (right panel) for $P_N = 20$ mTorr and $\alpha_{\text{coll}} = 100$. Plasma is injected to the system at the source region where $0.15 < x \leq 0.2$ m and the plasma collides with fixed neutral gas at $0 < x \leq 0.05$ m.

$\alpha_{\text{coll}} = 100$		
P_N (mTorr)	Δt (s)	N_g
0	8×10^{-13}	20,000
5	8×10^{-13}	25,000
10	8×10^{-13}	30,000
15	8×10^{-13}	70,000
20	5×10^{-13}	120,000

Table 4.3: Simulation parameters for time step size and the number of grid for $\alpha_{\text{coll}} = 100$.

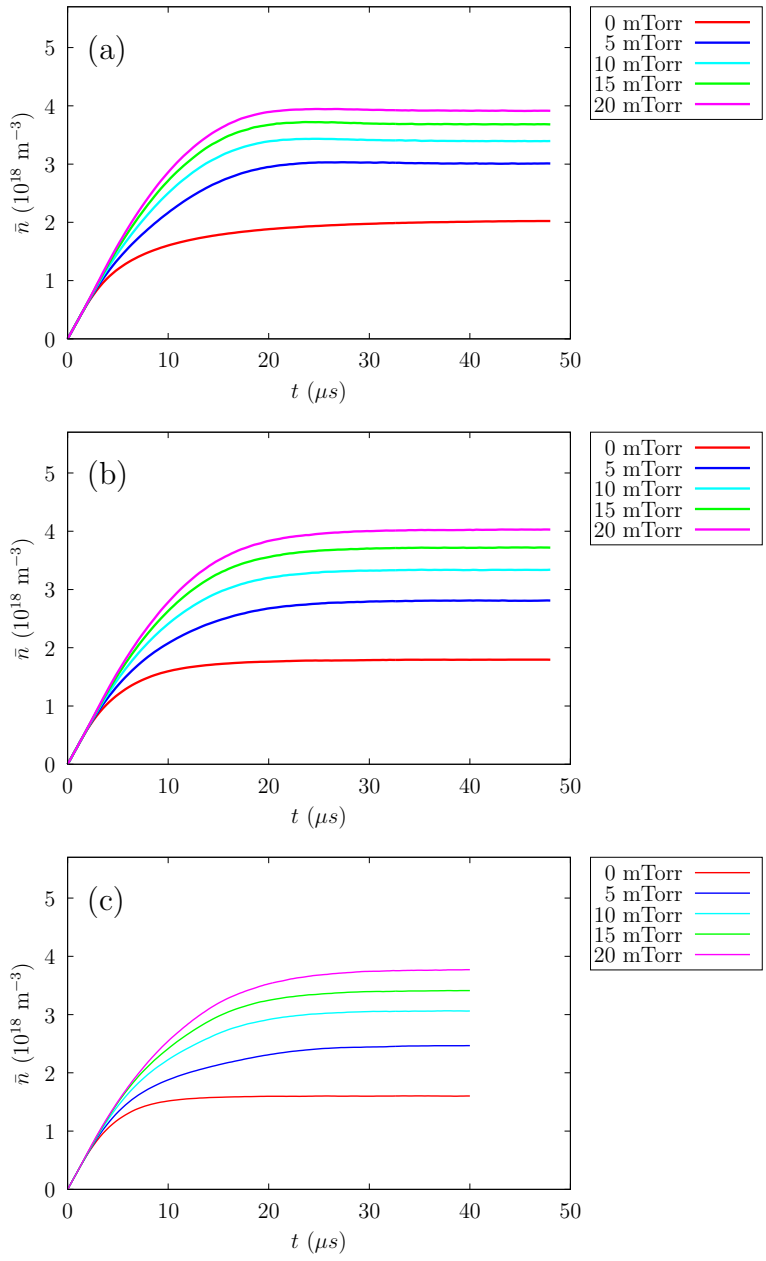

Figure 4.4: The time dependent plot of the average plasma density over the entire system with (a) $\alpha_{\text{coll}} = 1$, (b) $\alpha_{\text{coll}} = 10$ and (c) $\alpha_{\text{coll}} = 100$.

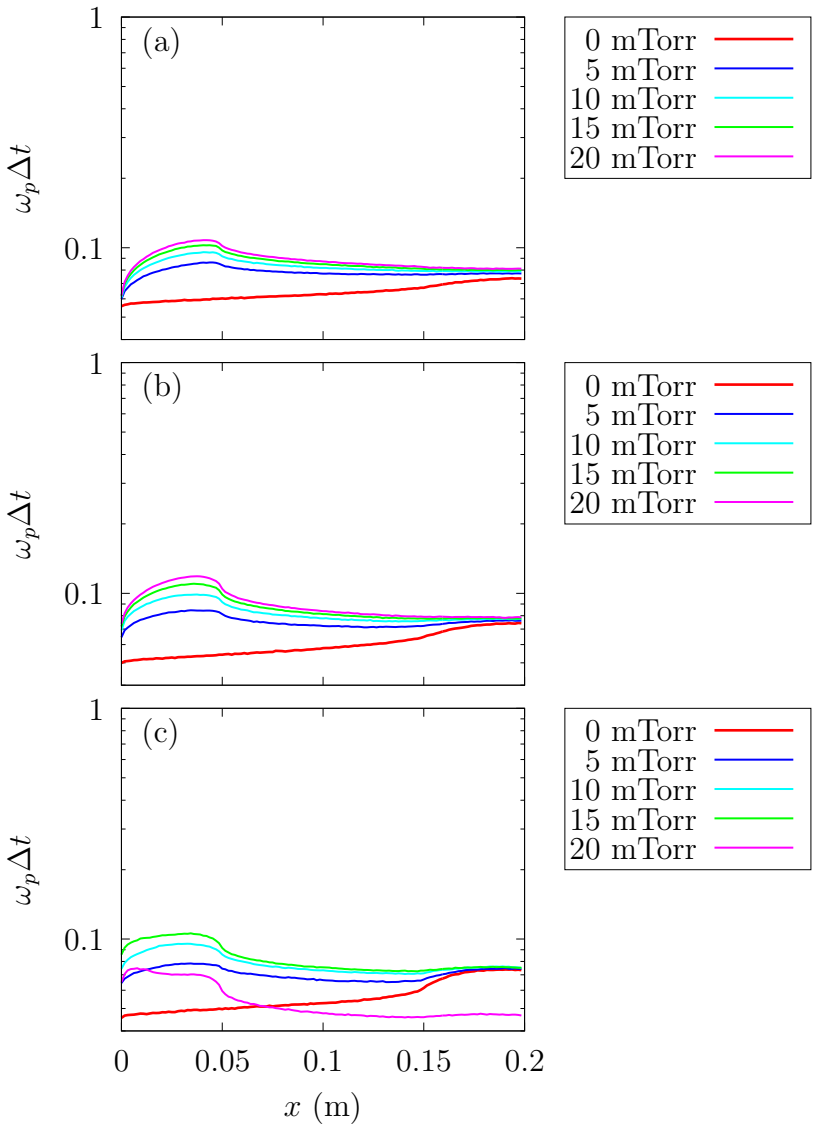

Figure 4.5: The spatial profile at the steady state of $\omega_p \Delta t$ for the case of (a) $\alpha_{\text{coll}} = 1$, (b) $\alpha_{\text{coll}} = 10$ and (c) $\alpha_{\text{coll}} = 100$.

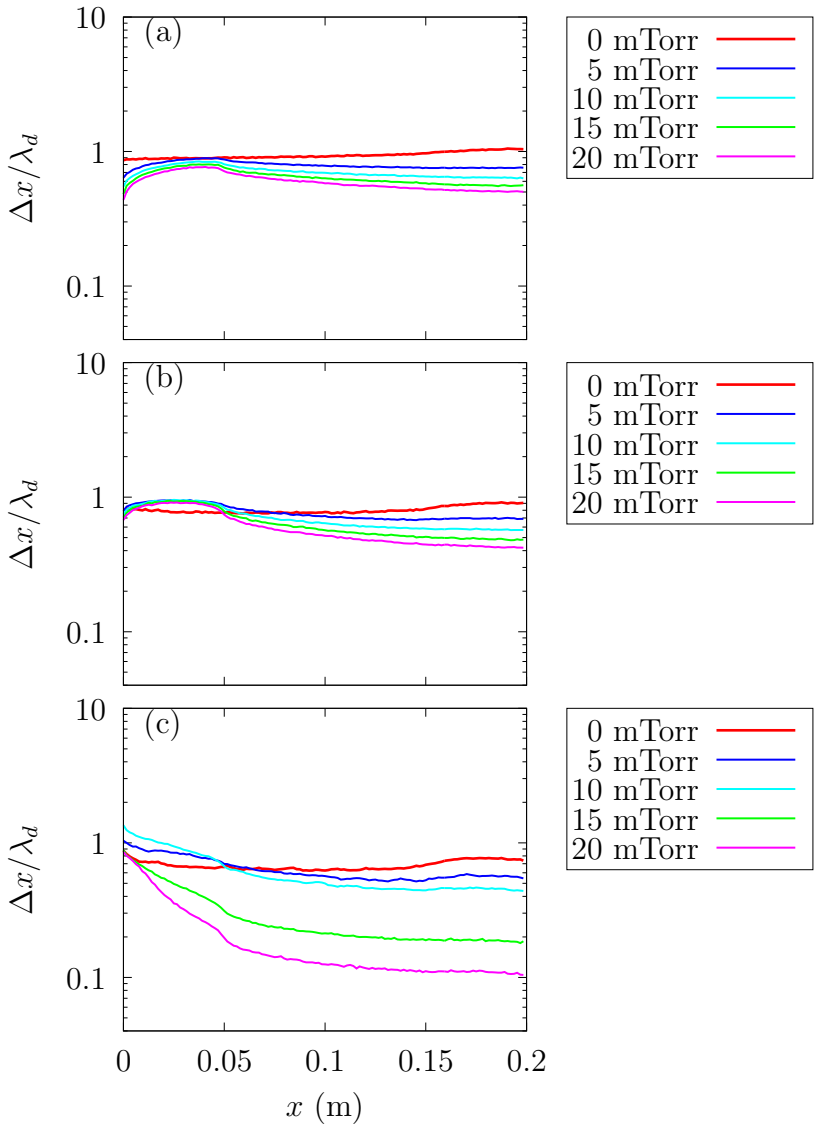

Figure 4.6: The spatial profile at the steady state of $\Delta x/\lambda_D$ for the case of (a) $\alpha_{\mathrm{coll}} = 1$, (b) $\alpha_{\mathrm{coll}} = 10$ and (c) $\alpha_{\mathrm{coll}} = 100$.

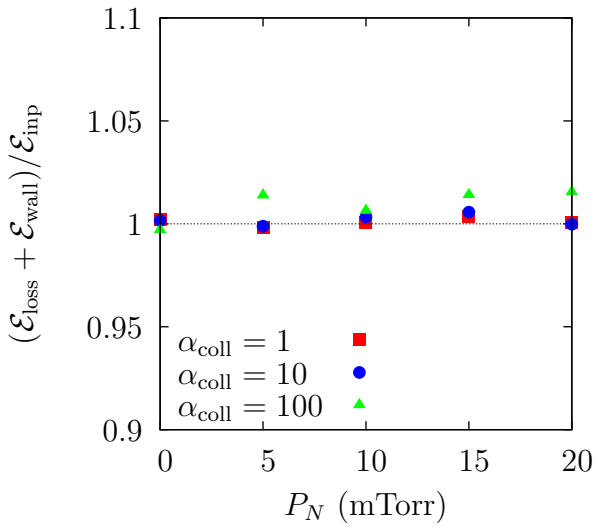

Figure 4.7: The dependent of the ratio of the sum of the energy loss by the atomic process $\mathcal{E}_{\rm loss}$ with the energy loss at the wall $\mathcal{E}_{\rm wall}$ over the total input energy $\mathcal{E}_{\rm inp}$ with the neutral gas pressure.

Chapter 5

The effects of neutral gas pressure on the SOL plasma

Neutral gas plays a key role in the plasma detachment process. Many experimental results show a strong relationship between the detached plasma and the neutral gas pressure in front of the divertor target.[6, 5] One of the key parameters for the formation of the detached plasma is the high plasma density which gives a strong reduction of plasma total pressure in front of the target.[66] The dependent of the strong reduction of the plasma total pressure with the plasma density means that the Coulomb collision mean free path need to be smaller or comparable to the system length. In this simulation, the modified Coulomb collision frequency is used to increase the effect of Coulomb collision to be able to compare with the experiment parameters. The Coulomb collision mean free path is estimated as $\lambda \sim 10^{16}T^2/n$. The mean free path over the system length of the linear device by using, the system length $L \sim 2$ m, the plasma temperature $T \sim 10$ eV and the plasma density $n \sim 10^{19}$ m^{-3} then becomes $\lambda/L \sim 0.05$. On the other hand, in our present simulation, $L \sim 0.2$ m, $T \sim 10$ eV and $n \sim 10^{18}$ m^{-3}. Then the ratio of $\lambda/L \sim 5$ which is different from the linear device parameter by a factor of 100. Thus, in this chapter, we set $\alpha_{\mathrm{coll}} = 100$ and investigate only the effect of the neutral gas pressure on the formation of the detached plasma.

5.1 Heat and particle fluxes in the detached plasma

Let us begin with brief explanation about our simulation model. As we have mentioned in the previous chapter, the neutral gas box is placed in front of the divertor target. We assume the uniform neutral gas with constant pressure and temperature. The dynamic of the neutral gas has not been included in our model. The neutral gas is also assumed to be in equilibrium, in which the distribution function is the Maxwellian and its temperature remains constant where $T_N = 0.1$ eV. Five simulations were performed, varying the neutral gas pressure P_N over the range $0 \leq P_N \leq 20$ mTorr.

The results of the characteristic of the detached plasma are displayed in Fig. 5.1. It indicates the strong reduction in the heat load to the target plate with the neutral gas pressure. The heat load is reduced greater than 10 times when $P_N = 20$ mTorr.

The main energy loss channel comes from the charge exchange process as shown in Fig. 5.2 where $\mathcal{E}_{\text{loss}}/\mathcal{E}_{\text{inp}}$ is the ratio of the amount of energy loss in each type of atomic process to the total input energy. Only small fraction of e-n collision processes contributes to the plasma cooling inside the neutral gas box due to the energy threshold for the excitation and ionization, in which the electron energy need to be greater than 10 eV to activate this channel. The energy loss caused by the ionization process is also much smaller than the excitation process because of the energy threshold is 13.6 eV which is larger than our source temperature. By using the cross-section data from our simulation, the rate coefficients of the atomic processes in our model are calculated. In Fig. 5.3, below approximately 5 eV the ionization and excitation rate coefficients are much smaller than the charge exchange, and the maximum values are given at approximately 100 eV, which is much higher than our source temperature.

Fig. 5.4 shows the comparison between particle fluxes, which are defined as the rate of change of the number of particles of each species over the area of the flux tube or $\Gamma = \Delta N/(A\Delta t)$ where $A = 1$ m^2. The particle fluxes from the source Γ_0 and from the ionization process Γ_{ion} are calculated from the particles that are created in each time step. The electron and ion are created in pair, thus electron and ion must have the same particle fluxes. The particle flux to the divertor target Γ_d is calculated from the number of particles that loss to the target and in the

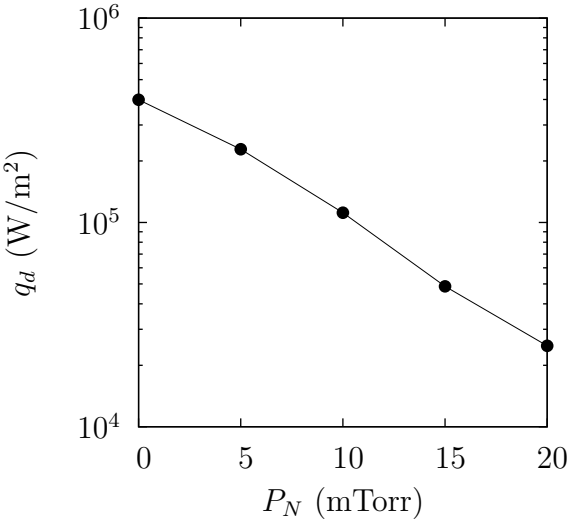

Figure 5.1: Heat flux to the divertor target vs neutral gas pressure at the steady state.

steady state electron and ion should reach the same particle flux to the target. In Fig. 5.4, the decrease in Γ_0 is caused by the reduction of the flow speed of the plasma at the downstream due to the ion-neutral collision. If we consider the ions flow to the wall suffering the ion-neutral collision, the particle flux is derived from the ambipolar diffusion[24], which shows that the particle flux to the target Γ_d decreases with decreasing ion-neutral collision mean free path λ_{in}:

$$\Gamma_d \propto \lambda_{in}/L. \tag{5.1}$$

In our simulation, the linear reduction of Γ_0 is observed. However, at low neutral gas pressure, the ionization flux increases when the neutral gas pressure increases because electron temperature does not decrease strongly in front of the target. Thus, Γ_d does not show significant reduction. After $P_N > 15$ mTorr, the Γ_{ion} starts to saturate which is affected by the electron temperature inside the neutral gas region drops sharply and causes the ionization front to move upstream.

5.2 Spatial structure of the detached plasma

In order to investigate the effect of the neutral gas on the detached plasma formation, the spatial profiles of plasma parameters are measured. Since the PIC simulation uses the real particle to simulate the plasma, the macroscopic plasma parameters of our interest need to be calculated by using the various order of the

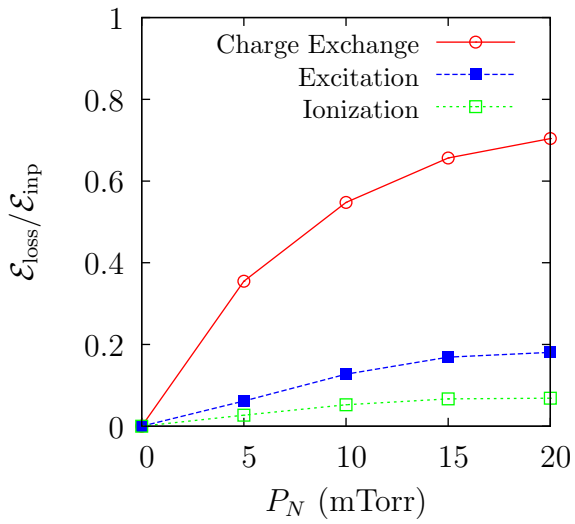

Figure 5.2: Energy loss of various atomic processes in the simulation at the steady state.

moment of the distribution function. The density n_s, the flow velocity $u_{k,s}$, the particle flux $\Gamma_{d,s}$, the temperature $T_{k,s}$ and the energy flux $q_{k,s}$ are calculated by

$$n_s(x) = \int_{-\infty}^{\infty} f_s(x,v)dv, \tag{5.2}$$

$$u_{k,s}(x) = \frac{1}{n_s(x)} \int_{-\infty}^{\infty} v_{k,s} f_s(x,v)dv, \tag{5.3}$$

$$\Gamma_{k,s}(x) = n_s u_{k,s}, \tag{5.4}$$

$$T_{k,s}(x) = \frac{1}{n_s(x)} \int_{-\infty}^{\infty} m_s(v_{k,s}^2 - u_{k,s}^2) f_s(x,v)dv, \tag{5.5}$$

$$q_{k,s}(x) = \int_{-\infty}^{\infty} v_{k,s} \frac{m_s v^2}{2} f_s(x,v)dv, \tag{5.6}$$

where s is species and $d = x, y, z$ is the component.

The spatial profiles of the transition from the attached state to the detached state are shown in Figs. 5.5. The system size is divided into 128 grids rather than using the real number of grid. This gives us the macroscopic structure for our simulation and also reduce the noise in the small cell.

In Figs. 5.5(a) and 5.5(b) the electron and ion parallel temperature profiles are shown respectively. For $P_N = 0$ mTorr case, a steep electron temperature gradient appears. For ions, the parallel temperature sharply drops at $x = 0.15$ m which is the boundary between the source and the source-free region. In the source region, the injected electrons have a larger thermal velocity than the injected ion. This gives rise to the source sheath drop. The ions are accelerated through the source

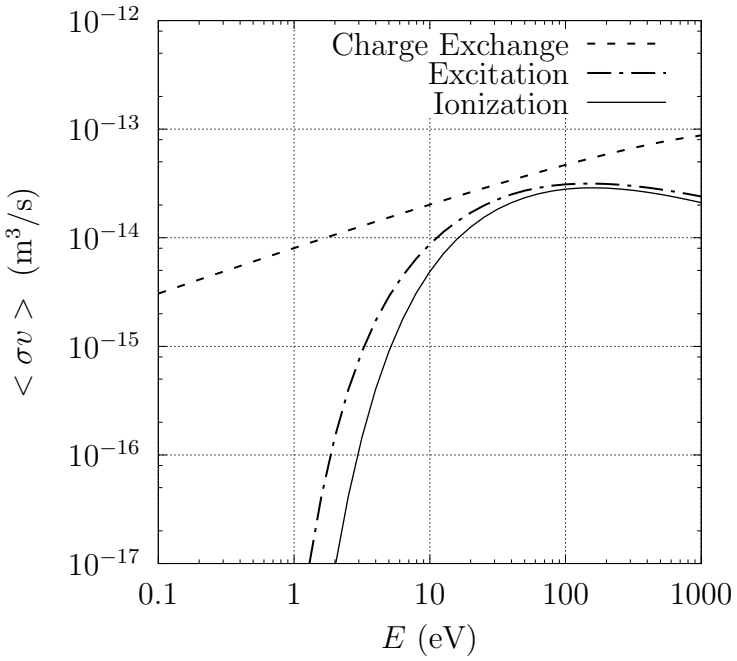

Figure 5.3: The rate coefficients of various atomic processes for the atomic hydrogen. Calculate by using the cross section data in Fig. 3.4.

sheath and the thermal velocity decreases. The ion parallel temperature gradient at $x > 0.05$ m is much smaller than the electron becayse the convection term of ion energy transport is dominate the conduction term. Inside the neutral gas region where $x < 0.05$ m, the steep electron temperature gradient appears when the neutral gas pressure becomes 15 mTorr. Ion temperature sharply decreases at the boundary of neutral source region where $x = 0.05$ m due to the ion-neutral collision and the step function of neutral density spatial profile. For $P_N = 20$ mTorr both electron and ion temperature reach the neutral gas temperature in front of the divertor. The perpendicular temperature profiles of the ion and the electron are plotted in Figs. 5.5(c) and 5.5(d) and the temperature profiles are almost isotropic with the parallel component due to the strong collisionality.

In Fig. 5.5(e), the spatial profile of plasma density is shown. The results show the constant upstream density $n_0 \approx 3 \times 10^{18}$ which was implemented in our model. For $P_N < 15$ mTorr, plasma density is peak near the ionization region which closes to the boundary of the neutral gas region. When the neutral pressure increases to 25 mTorr, the plasma density sharply increases to sustain the particle flux to the target due to the small temperature gradient in front of the target. The particle flux profiles are plotted in Figs. 5.5(f). Since the uniform

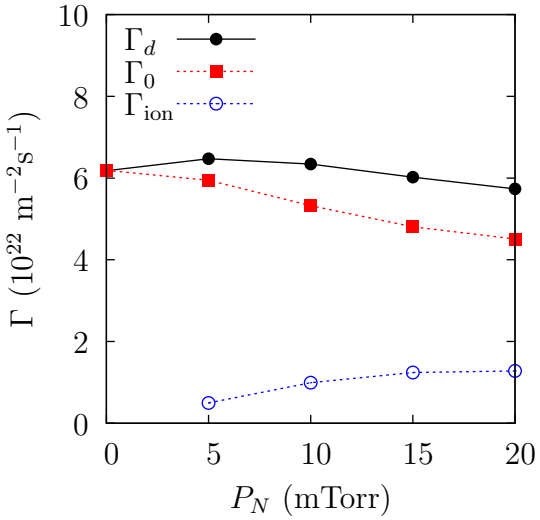

Figure 5.4: Particle flux to the divertor target Γ_d, particle flux from source region Γ_0 and particle flux from ionization region Γ_{ion} vs neutral gas pressure at the steady state.

distributed particle source is located at $x > 0.15$ m, the particle flux increases linearly in this region and becomes constant along the source-free region. The particle flux suddenly rises at $x = 0.05$ m which is the location of the electrons starts to ionize with the neutral gas. For $P_N = 5$ mTorr, the particle flux increases until reaching the target. However, for $P_N = 20$ mTorr, the particle flux increasing region becomes smaller due to the strong decrease in electron temperature which causes the ionization front to move upstream. The significant decrease in particle flux can not be seen because the recombination model or any particle sink term are not included in this work.

The ion flow speed profiles are exhibited in Fig. 5.5(g). The reduction of the ion flow when increasing the neutral gas pressure can be observed. For $P_N = 0$ mTorr, the flow speed increase along the x-direction. However, for $P_N > 0$ mTorr, the flow speed gradually decreases along the source-free region and then suddenly increase near the target. The Mach number profiles are plotted in Fig. 5.5(h), where $M = u_{||,i}/c_s$ and $c_s = \sqrt{(kT_e + kT_i)/m_i}$ is the local ion acoustic speed. For $P_N = 0$ mTorr, $M \approx 1$ at the entrance of the source-free region and $M > 1$ until reaching the target. This is due to the source sheath drop as has been discussed in the results of the ion parallel temperature. Procassini et al. [42] also showed the similar result by using the implicit PIC simulation. For $P_N > 0$ mTorr, M becomes subsonic along the source free region and sharply increase inside the

neutral gas region to reach the supersonic flow at the target. The supersonic flow before reaching the target is seen for $5 \leq P_N \leq 20$ mTorr. This may be caused by the ionization source inside the neutral gas region creates the source sheath drop near the target.

The total pressure profile is shown in Fig. 5.5(i). The total pressure is the sum of both dynamic and static pressure, where

$$P_{\text{tot}} = n(m_i u_i^2 + kT_i + kT_e). \tag{5.7}$$

Inside the neutral gas region where $x < 0.05$ m, the reduction of the total pressure is shown when $P_N > 0$ mTorr. To look into more details, we can refer to the the momentum balance equation:

$$\frac{d}{dx} P_{\text{tot}} = -m_i u_i \langle \sigma v \rangle_{in} n n_n. \tag{5.8}$$

In the case of $P_N = 0$ mTorr, the total pressure should be constant because of no momentum loss in the system and this is exhibited in Fig. 5.5(d). When $P_N > 0$, ion-neutral collision causes the total pressure to decrease inside the neutral gas region. The total pressure gradient becomes larger as P_N increases. The total pressure strongly decreases and approach to zero in front of the target in the case of 20 mTorr. The upstream pressure increases as the neutral gas pressure increases. The static pressure profiles are shown in Fig. 5.5(j) where $p = nkT_i + nkT_e$. The decrease in the ion flow speed outside the neutral gas region causes the static pressure increase.

The structure of presheath and sheath are obtained in our simulation. The sheath is the structure on the scale of the Debye length λ_D and plasma frequency ω_p. Thus, the fully kinetic model is necessary to obtain the sheath potential profile directly. The results of the potential profile which shown in Figs. 5.6 is obtained by averaging over time after the steady state by the interval of $200{,}000\Delta t$. This reduces the fluctuation of the potential structure. The strong potential drop inside the neutral gas region is found and the gradient increases when the neutral pressure increases. The potential drop across the collisional zone can be expressed by [24]

$$e\Delta V / kT_e \approx -\ln(L/\lambda_{in}). \tag{5.9}$$

This relation shows that when the ion-neutral mean free path becomes smaller the potential drop becomes larger. Our simulation also shows the large potential drop in high neutral gas pressure.

5.3 Kinetic effects inside the SOL

The ion and electron distribution functions at the target are shown in Fig. 5.7. The distribution function is calculated at the last cell by averaging over time after the steady state by the time interval of $20,000\Delta t$. The effect from the sheath potential drop at the target on the distribution function is clearly shown in Figs. 5.7(a) and 5.7(b). Electron distribution function is cut off due to the sheath potential drop and the part of the upstream direction tail is cut off. The ion distribution shows the supersonic flow of ion at the wall which causes by the acceleration of ion to the sheath. This acceleration tends to narrow the velocity distribution function more for $P_N = 5$ mTorr. The drift velocities compare with the acoustic speed become smaller when the neutral gas pressure increases.

Kinetic effects is not clearly observed in this work because we assume the Maxwellian distribution function for the background neutral thus the strong i-n collision tends to lead the ion distribution function to become Maxwellian. The kinetic model for the neutral transport is necessary for fully understanding of the kinetic effects.[32]

5.4 Dynamics of the detached plasma

We have seen the strong reduction of the heat flux causes by the neutral gas pressure in Fig. 5.1. The time dependent of the heat flux at the target is shown in Fig. 5.4. Shortly after the simulation has started, the heat flux strongly increases due to the free streaming of the plasma flow directly to the wall. The heat flux becomes saturate later on. If $P_N > 15$ mTorr, the heat flux decreases before reaching the steady state.

The time evolution of the spatial profile of plasma quantities at $P_N = 20$ mTorr are displayed in Fig. 5.9. At $t = 4$ μs, the heat load starts to decrease from the maximum point. Electron temperature is larger than the ion temperature. At $t = 8$ μs, the heat flux strongly decreases and electron temperature approaches the ion temperature. The plasma density starts to increase in front of the target. After $t = 8$ μs, (1) the heat flux saturates, (2) the electron temperature is almost equal to the ion temperature, and (3) the plasma density peak moves downstream. The e-i energy relaxation process transfers the energy from electron to ion, then ion

loses the energy by the charge exchange process and leads to the strong reduction of the heat fluxes to the target. It is interpreted that the Coulomb collision effect plays an important role in the strong reduction of the heat flux to the target, and more results are presented in the next chapter.

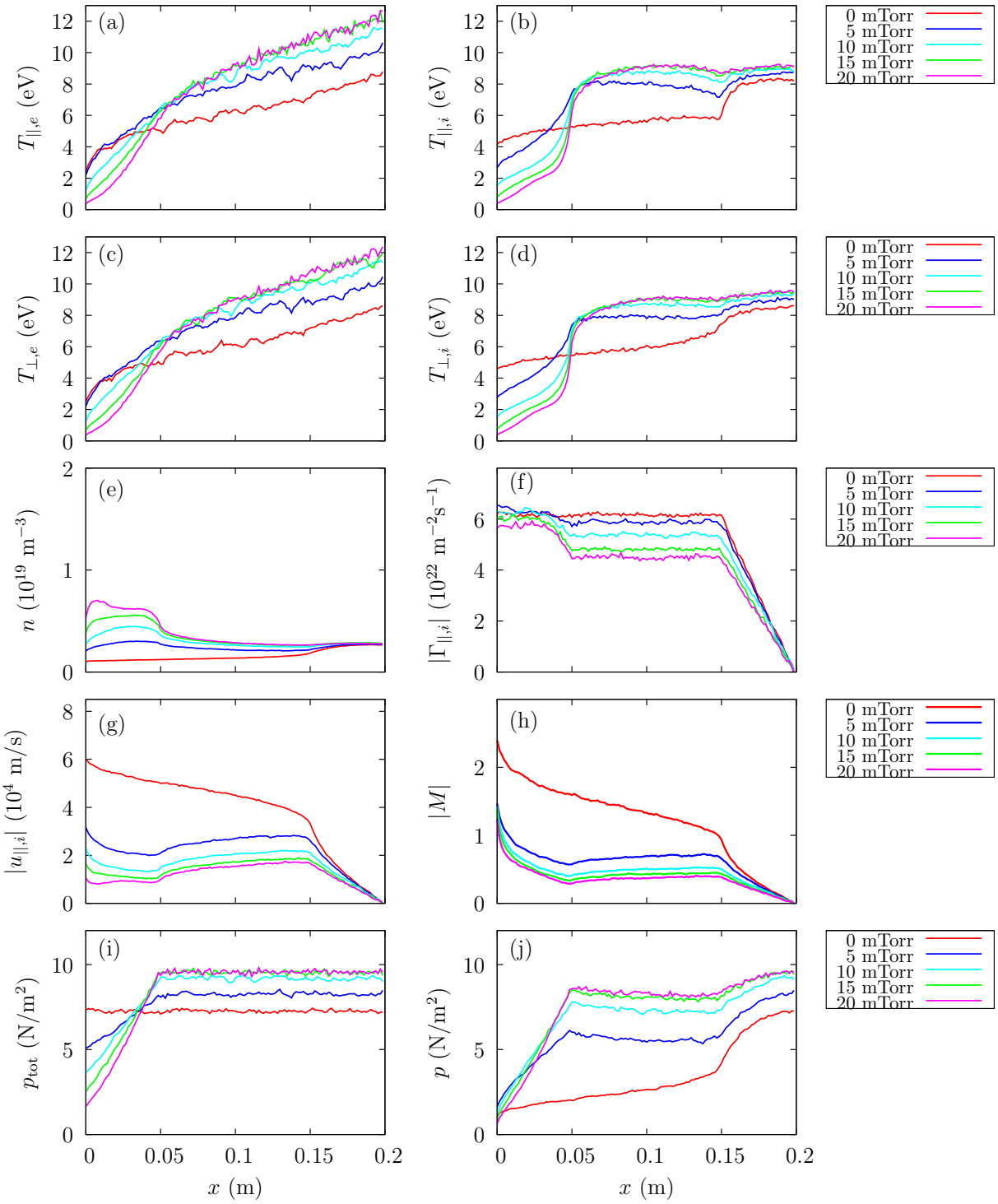

Figure 5.5: Spatial profile at the steady state of (a) parallel electron temperature, (b) parallel ion temperature, (c) perpendicular electron temperature, (d) perpendicular ion temperature, (e) plasma density, (f) ion parallel particle flux, (g) ion parallel flow speed, (h) Mach number, (i) total plasma pressure, and (j) static plasma pressure.

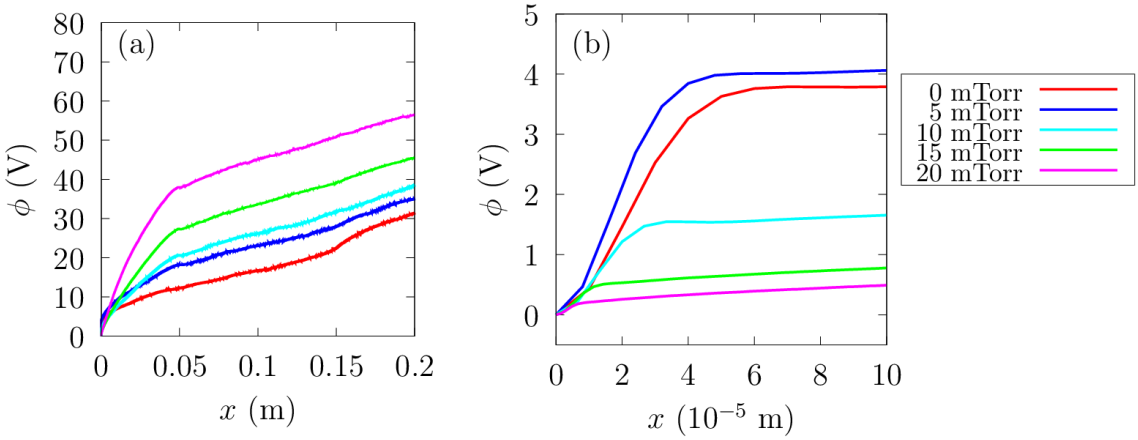

Figure 5.6: Spatial profile of the electro static potential at the steady state for (a) the overall system (b) near the sheath region.

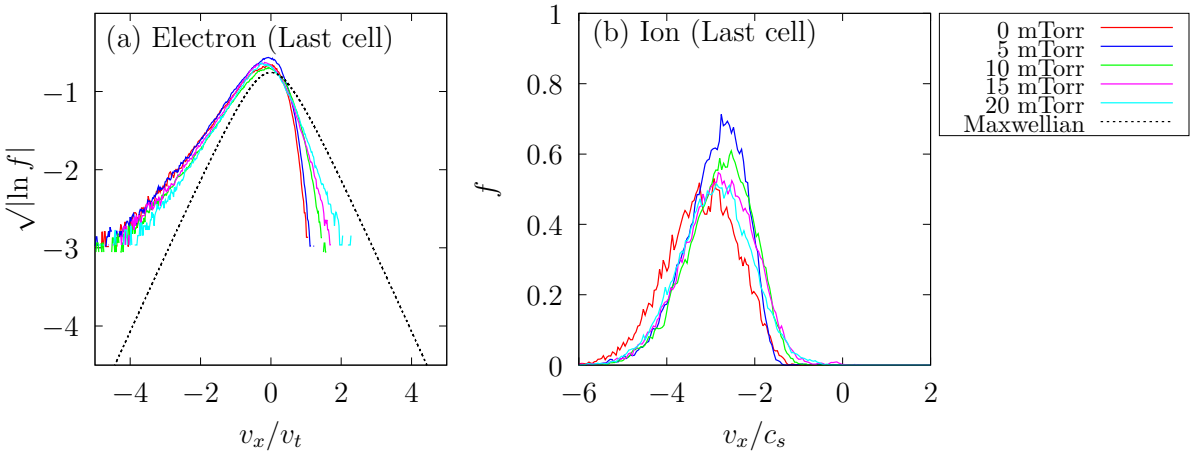

Figure 5.7: Electron and ion distribution function at the last cell. The negative velocity shows the particles that move toward the target and the positive velocity shows the particles that move toward the midplane.

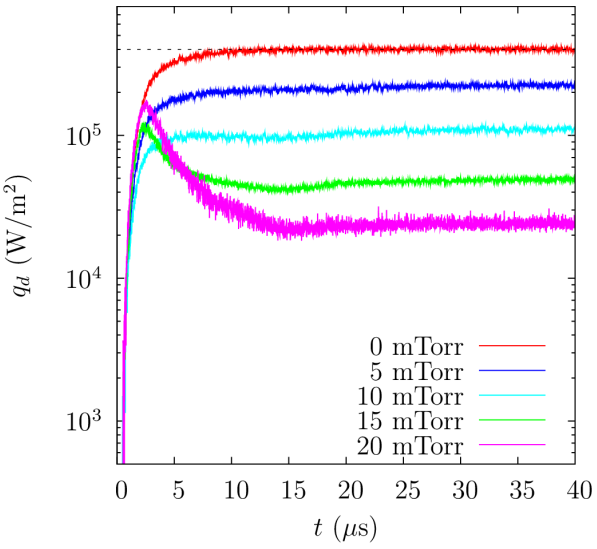

Figure 5.8: Time evolution of the heat flux to the target.

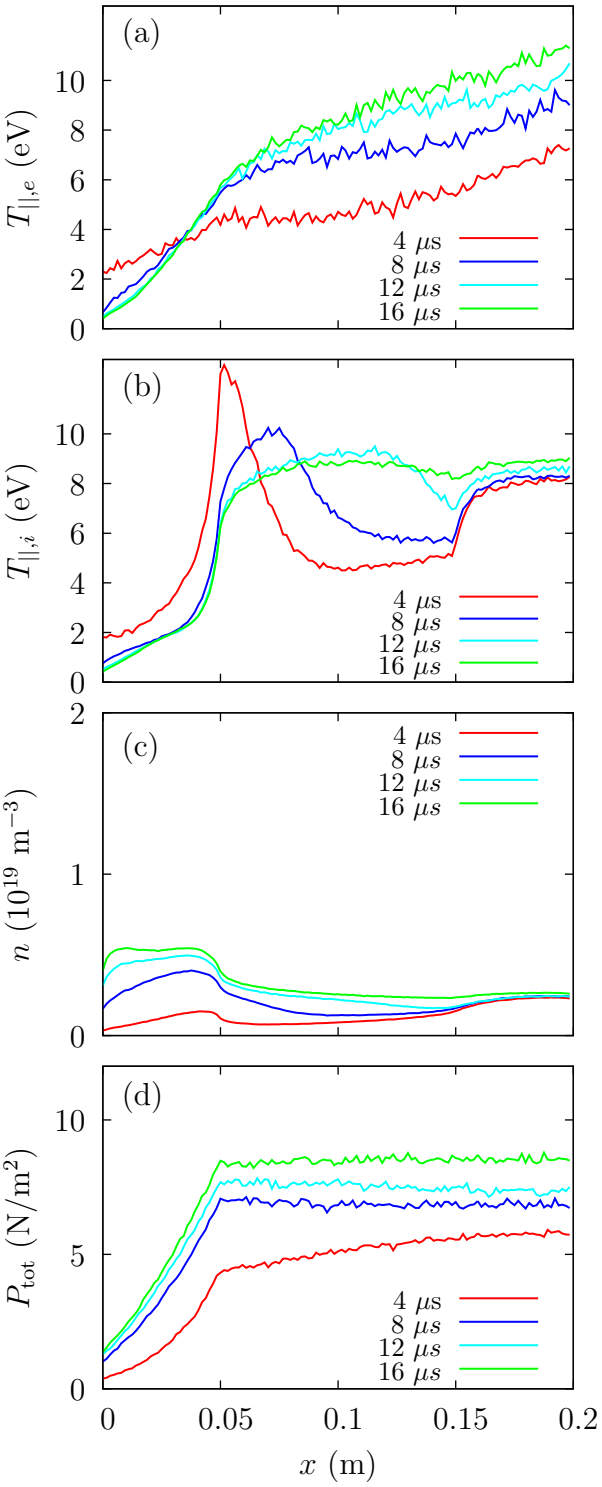

Figure 5.9: Time dependent spatial profile at $P_N = 20$ mTorr of (a) parallel electron temperature, (b) parallel ion temperature, (c) density, (d) total plasma pressure.

Chapter 6

The Effects of Coulomb collision on the SOL Plasma

The Coulomb collisionality is defined as $\nu^* \equiv \nu_{c0}/\nu_{be0}$, where ν_{c0} is the Coulomb collision frequency between ion and electron from the source region and ν_{be0} is the bounce frequency where $\nu_{be0} = v_{te0}/L$ and v_{te0} is the source electron thermal velocity. These give $\nu^* \sim 10^{-16} n_u L/T_{e0}^2$ (T_{e0} in eV, n_u in m^{-3}, and L in m). In this simulation, the collisionality is determined by α_{coll} and the effect of the collisionality with the SOL plasma has been studied in previous work of PIC simulation.[8, 9]

In chapter 5, the strong reduction of the total heat flux when neutral gas pressure increase to several millitorr is shown. The formation of the detached plasma is observed at $P_N = 20$ mTorr. However, only the results of $\alpha_{\mathrm{coll}} = 100$ are shown. In this chapter, the effect of the collisionality on the formation of the detached plasma will be discussed with the results from the PIC simulation.

6.1 Collisionality effect on the heat transport

Fig. 6.1 shows the dependence of heat flux on the neutral gas pressure, where q_d is the total heat flux of the plasma at the target. The results show that for the moderate to low collisionality $\alpha_{\mathrm{coll}} < 10$, the heat flux decreases less than one order of magnitude. However, when $\alpha_{\mathrm{coll}} = 100$ the strong reduction is clearly observed. In the linear device experiment[66], it was shown that the heat flux reduction ratio q_d/q_{inp} has a strong dependence with the plasma density and the

energy removal by neutral gas becomes weak at low plasma density. The relation between plasma density and Coulomb collision frequency is written as

$$\nu_c = \frac{\ln \Lambda}{4\pi} \left(\frac{q_\alpha q_\beta}{\varepsilon_0 \mu_{\alpha\beta}} \right)^2 n v_{Te}^{-3}. \tag{6.1}$$

The collisional acceleration factor $\alpha_{\rm coll}$ is used to increase the collision frequency rather than increase the density. The dependence of $\alpha_{\rm coll}$ with the heat flux reduction rate is shown in Fig. 6.2. The strong reduction of $q_d/q_{\rm inp}$ at high value of $\alpha_{\rm coll}$ is displayed. The simulation gives a good agreement with the experiment results.

The mechanism of energy loss is explained by the energy loss channel in various atomic processes. Figs 6.3 shows the ratio of the amount of energy loss in each type of atomic process to the total energy input $\mathcal{E}_{\rm loss}/\mathcal{E}_{\rm inp}$ which varies by neutral gas pressure. Since our model heats the only electron inside the source region, at $\alpha_{\rm coll} = 1$, the energy loss from the excitation becomes dominate. But when $\alpha_{\rm coll}$ increases, the energy loss from the charge exchange process becomes larger. In the high collisionality case with $P_N = 20$ mTorr, almost 70% of energy loses from the charge exchange process. The ionization process does not have any significant role for the energy loss.

The energy flow diagram as shown in Fig. 6.4 illustrates the mechanism of the energy loss channel inside the detached plasma. The excitation and ionization processes are not so effective for cooling T_e below 5 eV. The removal of energy from electron below 5 eV is mainly caused by the e-i energy relaxation process. The energy relaxation time is calculated from

$$\tau_{ie} = \frac{3\sqrt{2\pi}\epsilon_0^2 m_e^{-1/2} m_i T_e^{3/2}}{n_e Z^2 e^4 \ln \Lambda}, \tag{6.2}$$

where Z is the ionic charge number. The particle confinement time inside the system is estimated as $\tau_p \sim L/c_s$. The plasma parameters in our simulation are $T_e \sim 10$ eV, $n_e \sim 10^{18}$ m^{-3} and $L = 0.2$ m. These parameters give a large value of $\tau_{ie}/\tau_p \sim 53$. The energy relaxation time of this simulation is calculated as $\tau'_{ie} = \tau_{ie}/\alpha_{\rm coll}$. If $\alpha_{\rm coll} = 100$, the ratio of the energy relaxation with the particle confinement time $\tau'_{ie}/\tau_p \sim 0.53 < 1$, which gives strong coupling between electron and ion by the Coulomb collision inside the system.

The time dependence of the strong reduction shows no different in the case of $P_N = 0$ mTorr because the plasma flow is free stream from the target to

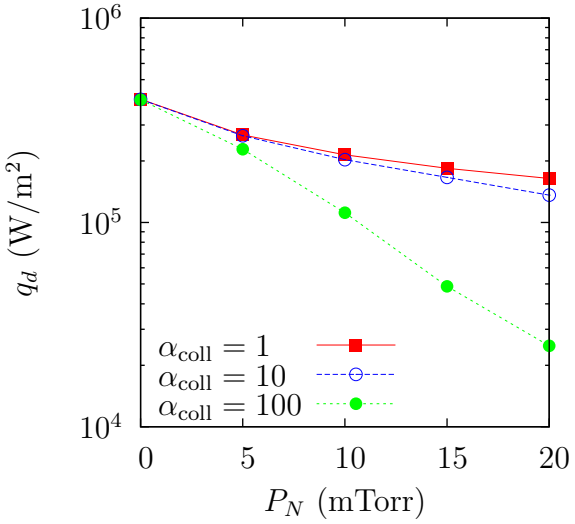

Figure 6.1: The dependence of the total plasma heat flux at the divertor target q_d on the neutral gas pressure P_N at the steady state, where q_d includes both electron and ion heat flux at the target.

the wall as exhibited in Fig. 6.5(a). However, the reduction of the heat flux is observed in Fig. 6.5(b) in the high collisionality case. As we already explained in the previous chapter, during the e-i relaxation process heat flux to the target decreases. However, in the low collisionality case, the reduction of heat flux is not observed due to the lack of the e-i coupling by the Coulomb collision.

6.2 Spatial structure of physical quantities

For $P_N = 0$ mTorr, the spatial profiles from different collisionality are shown in Figs. 6.6. The perpendicular and parallel temperature profiles for electron and ion are shown in Figs. 6.6(a)-(d). The temperature gradient becomes larger as the collisionlity increasing. The decrease in energy relaxation time between electron and ion leads to the increase in electron temperature at the upstream. In Figs. 6.6(e)-(j), the ion flow speed becomes larger when the collisionality increases and the density becomes smaller so that the particle flux is conserved inside the source free region.

For $P_N = 20$ mTorr, Figs. 6.7(a)-(d) shows that the collisionality leads to the increase in electron temperature gradient at the source free region. The dramatic decrease in electron temperature near the target is clearly seen for $\alpha_{\rm coll} = 100$. In our model, only electrons are heated in the source region, thus in low collisionality,

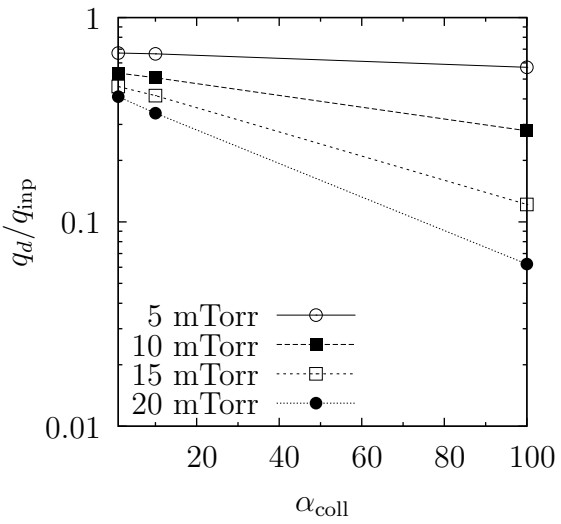

Figure 6.2: The dependence of the collisional acceleration factor with the heat flux reduction ratio.

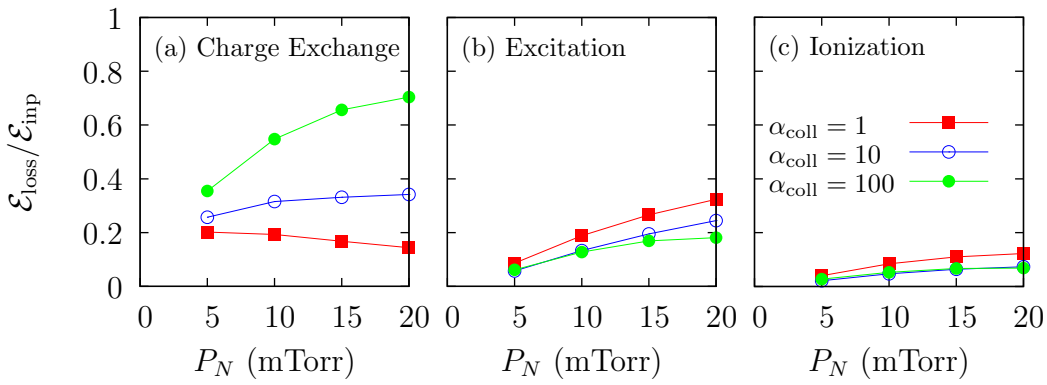

Figure 6.3: The variation of the the ratio of energy loss to energy input by (a) the charge exchange, (b) the excitation and (c) the ionization with the neutral gas pressure.

due to the small energy exchange between electron and ion, the ion temperature inside the source region becomes smaller. The particle flux for $\alpha_{\rm coll} = 1$ or 10 increases along the source region until reaching the target, however for $\alpha_{\rm coll} = 100$, the particle flux increases only in a small region near the boundary of neutral gas box $x = 0.05$ m. This is because the ionization front moves to the upstream in the high collisionality case, thus reducing the plasma source region from the ionization process. The flow velocity of ion near the target is larger in the low collisionality case.

The spatial profiles of the electrostatic potential from Fig. 6.8 shows the

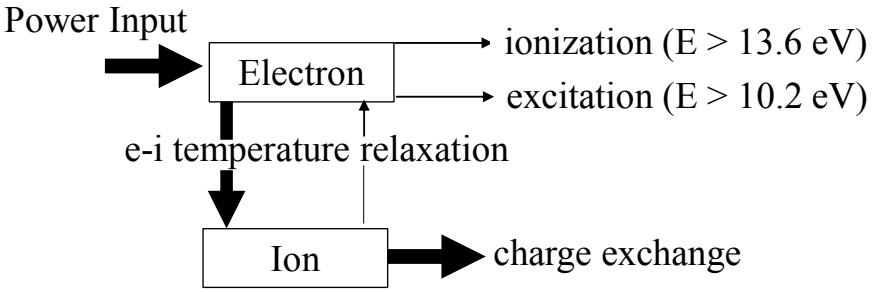

Figure 6.4: Energy flow diagram for the energy loss in the neutral gas region during the detached state. The arrows indicate the energy transfer in which the electrons mainly transfer their energy to ion, then the charge exchange process dominates the cooling of the plasma temperature.

increase in potential drop when the collisionality increases. For $P_N = 20$ mTorr, the small peak of the potential profile is exhibited due to the ionization source at the boundary of the neutral gas box. Electrons created by the ionization process tend to move faster than the ion and leave to positive charge density inside this region.

6.3 Kinetic effects

Electron distribution functions are shown in Figs. 6.9(a) and 6.9(c). In the low neutral pressure case, Electron distribution function is cut off due to the sheath potential drop and the part of the upstream direction tail is cut off. However, in high neutral gas pressure case, the deviation is observed in the low collisionality case and vanish in the high collisionality case.

The ion distribution functions shown in Figs.6.9(b) and 6.9(d) are far from the Maxwellian distribution in the low collisionality case. In the high collisionality case, the strong plasma density peak that locates near the target causes the increase in the Coulomb collision frequency then the distribution function approach to the Maxwellian.

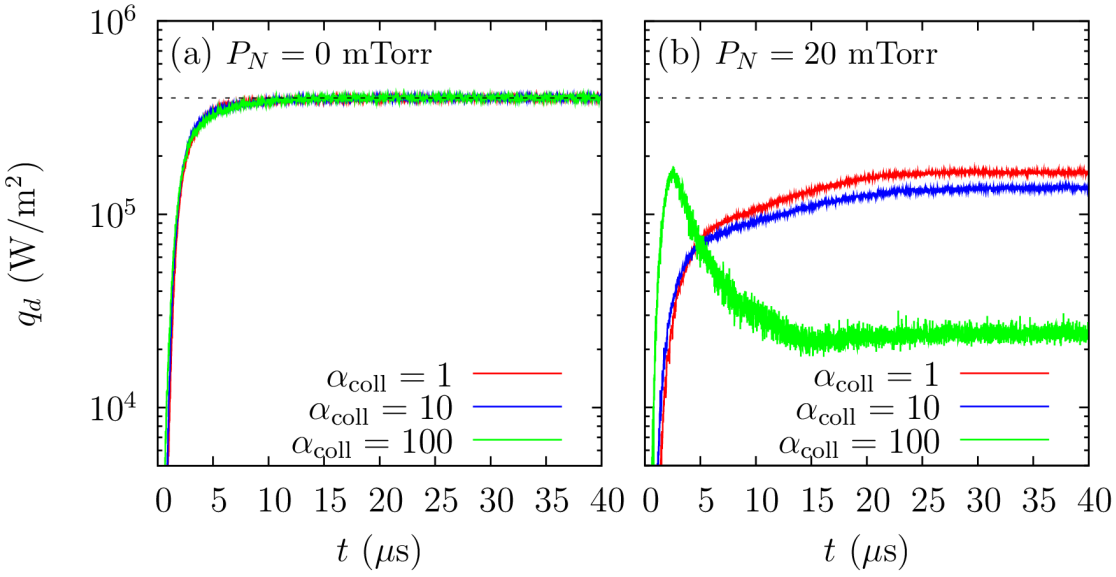

Figure 6.5: Time evolution of the total plasma heat flux q_d at the divertor target.

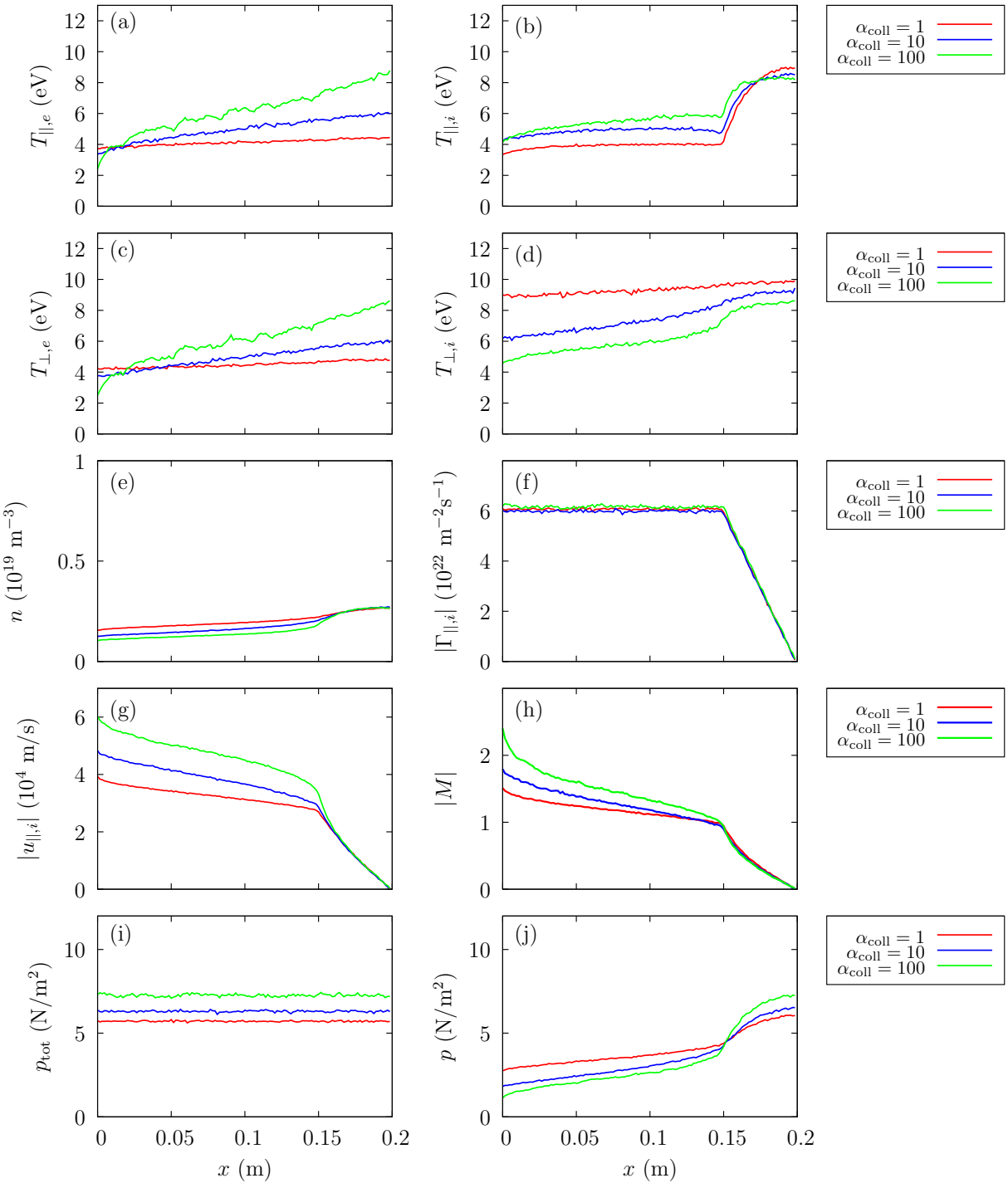

Figure 6.6: Spatial profile at the steady state of (a) parallel electron temperature, (b) parallel ion temperature, (c) perpendicular electron temperature, (d) perpendicular ion temperature, (e) plasma density, (f) ion parallel particle flux, (g) ion parallel flow speed, (h) Mach number, (i) total plasma pressure, and (j) static plasma pressure for $P_N = 0$ mTorr

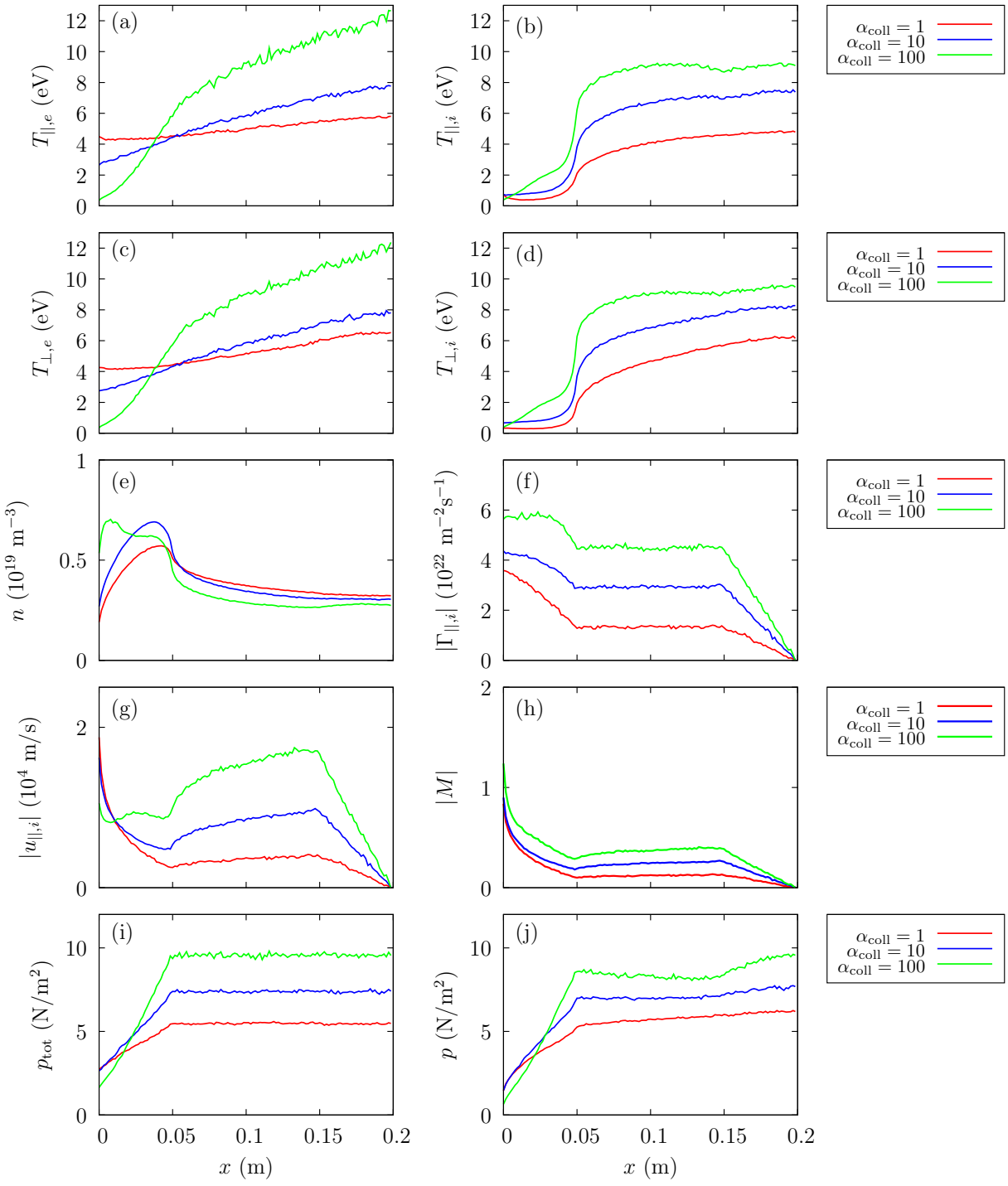

Figure 6.7: Spatial profile at the steady state of (a) parallel electron temperature, (b) parallel ion temperature, (c) perpendicular electron temperature, (d) perpendicular ion temperature, (e) plasma density, (f) ion parallel particle flux, (g) ion parallel flow speed, (h) Mach number, (i) total plasma pressure, and (j) static plasma pressure for $P_N = 20$ mTorr

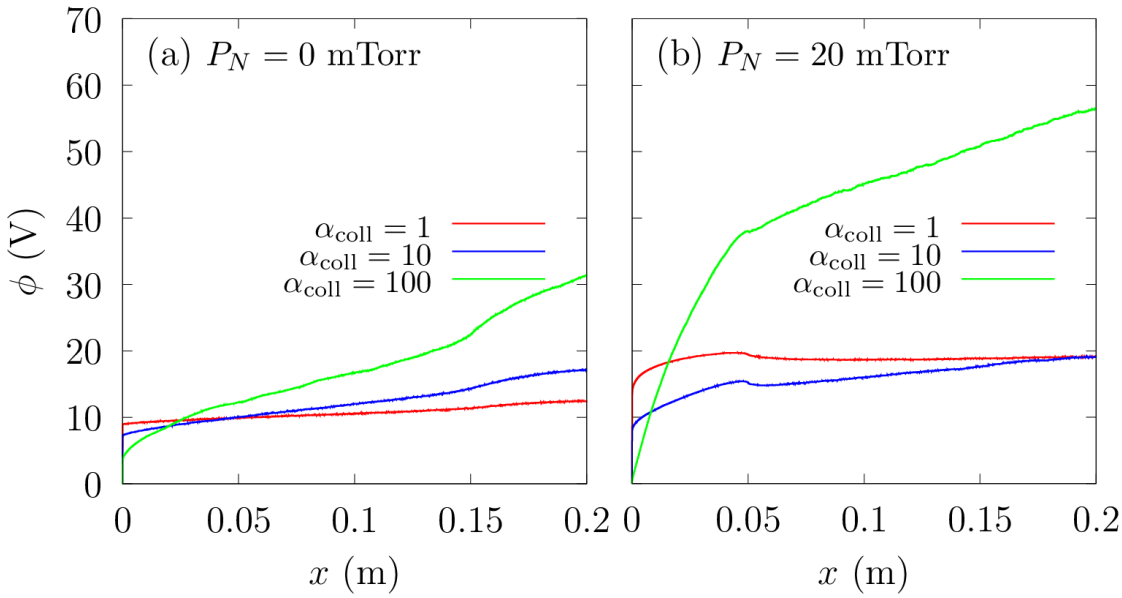

Figure 6.8: Spatial profile of the potential structure for (a) $P_N = 0$ mTorr and (b) $P_N = 20$ mTorr.

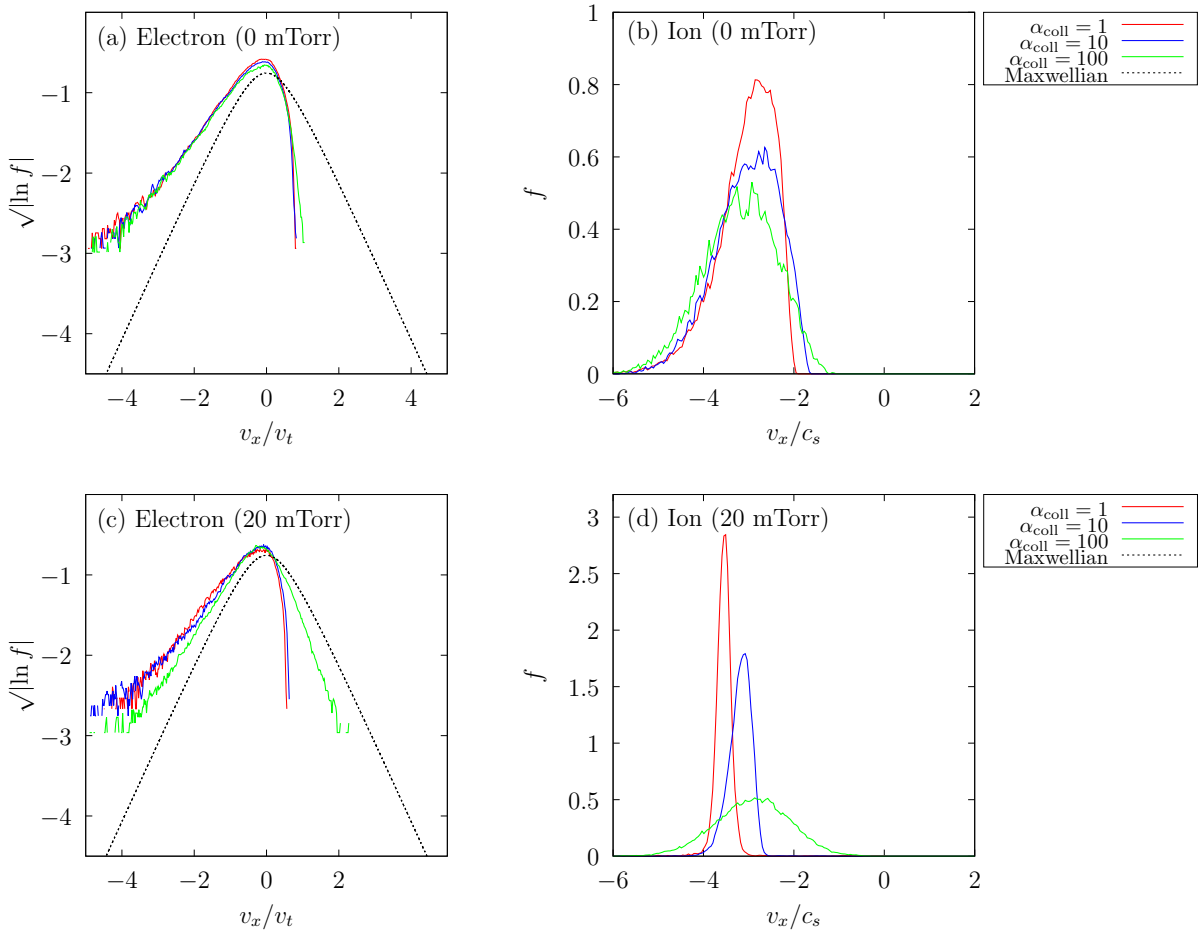

Figure 6.9: The distribution function at the target of (a) electron for $P_N = 0$ mTorr, (b) ion for $P_N = 0$ mTorr, (c) electron for $P_N = 25$ mTorr, and (d) ion for $P_N = 25$ mTorr. The negative velocity shows the particles that move toward the target and the positive velocity shows the particles that move toward the midplane.

Chapter 7

Conclusion and discussion

The results of the plasma detachment formation are presented in our study. In order to study the kinetic effect on the formation of the detached plasma, we have developed a PIC-MCC simulation, which is the fully kinetic self-consistent model, by using the high-performance parallel computing. In this model, the Coulomb, i-n and e-n collisions are included. The simulation is performed in a large system size up to hundred thousand Debye length in which the results approach the real experiment values. The sheath structure which is one of the most important issues for the plasma-wall interaction is treated self-consistently. We assumed the uniform neutral gas box in front of the target which resembles the linear devices.

The simulation parameters are selected to give the results that are compared to the linear device experiment. We modified the collisionality to be in the same order as in the linear device. The neutral gas pressure is varied to show the formation of the detached plasma. We also studied the dependence of the collisionality on the formation of the detached plasma. The spatial structures of the physical quantities are investigated in both cases.

The feature results of this work are concluded as follows:

1. By fixing the neutral gas temperature and pressure, the results of the exponentially decrease in heat flux to the divertor target when increasing the neutral gas pressure is obtained. These results show the same trend with the real experiment in the linear devices in which the neutral gas is used for absorbing both momentum and power from the plasma. The effect of the sheath on the ion and electron heat fluxes are found. Since the real mass ratio is used in this work, the ion heat flux is much larger than the electron

heat flux and the ion heat flux strongly depends on the electron temperature. For the energy loss, the main channel for our model is the charge exchange and this channel is much higher than the e-n collision because of the source temperature is assigned to 10 eV. The strong reduction of the particle flux to the target is not found. These results show that the recombination process must play an important role in the detached plasma.[67]

2. The strong electron temperature gradient in front of the divertor target is observed in a high neutral gas pressure condition. The electron temperature approaches the neutral gas temperature and almost constant near the target. The plasma density peak shift from the ionization front toward downstream to the location where electron temperature almost constant. This mechanism is affected by the particle flux conservation along the magnetic field line. Due to the strong decrease in the temperature gradient near the plate during the detached state, the density gradient must rise sharply. The total plasma pressure drops sharply in front of the target due to the strong energy and momentum removal caused by the i-n collision.

3. The effect from the sheath potential drop at the target on the distribution function is found. Electron distribution function is cut off due to the sheath potential drop and the part of the upstream direction tail is cut off. The ion distribution shows the supersonic flow of ion at the wall which is caused by the acceleration of ion through the sheath. The drift velocities compare with the acoustic speed become smaller when the neutral gas pressure increases. The deviation from the Maxwellian is observed. However, at high P_N and high collisionality, the sharp rise of the plasma density in front of the target increases the Coulomb collision frequency and reduce the deviation.

4. The dynamic of the detached plasma formation is exhibited in our work. The time dependence of the heat flux to the target shows the sharp decrease when electron temperature relaxes toward the ion temperature. This is the evidence of the Coulomb collision effect on the formation of the detached plasma.

5. In the low collisionality case, the detached plasma is not observed and even in high neutral gas pressure, the heat flux to the target is much larger than

the high collisionality case. The electron temperature and total plasma pressure do not show any significant drop. Only the ion temperature strongly decreases. The plot between the ratio of the heat flux at the wall to the input heat flux with the collisionality shows the consistent results with the linear device. The reason behind this is the e-n collision process almost vanish when the electron temperature goes below 5 eV. Thus in our model, the electron temperature will never go below 1 eV without the effect from the Coulomb collision process.

We need to remark that even though we observe the detached plasma by using the 1D-3V PIC simulation other types of atomic processes may become important for study the effect of the detached plasma. In our parameters selection, the source temperature is around 10 eV thus we neglected the impurity radiation in our model but for the case of the upstream temperature around 100 eV, the impurity radiation becomes important. When plasma temperature goes below 1 eV the recombination process becomes important for the strong removal of the particle flux. The MCC model for a given rate constant is used to treat the recombination process.[68, 69] Another point is the dynamic of the neutral transport, which is important in understanding the detached plasma.[32, 70] In our present work, the neutral particles fully absorbed all the energy from the plasma. However, this high energy neutral directly spread the local heat flux to the target and increases the total heat flux at the target.

Appendix A

Sheath formation by planar source model

The planar source model as in Fig. A.1 is used to verify the sheath formation in the simulation code when there is no collision processes occur.[71] The boundary condition on the left hand side is assumed with the fully absorbed wall with floating potential and the right hand side is assumed with the fixed potential. The flux injection distribution $v_x f(v_x) dv_x$ is use for the particle injection from the right-hand wall, where f is Maxwellian distribution. Ion and electron are injected from the plane on the right hand side with a constant flux. The theoretical model is explained below.

The accelerated Maxwell-Boltzmann distribution function under the electrostatic potential ϕ is

$$f_e(\phi, v) = n_{e0}\left(\frac{m_e}{2\pi k T_{e0}}\right)^{1/2} \exp\left(-\frac{m_e v^2}{2kT_{e0}} + \frac{e\phi}{kT_{e0}}\right) \tag{A.1}$$

$$f_i(\phi, v) = n_{i0}\left(\frac{m_i}{2\pi k T_{i0}}\right)^{1/2} \exp\left(-\frac{m_i v^2}{2kT_{i0}} - \frac{e\phi}{kT_{i0}}\right) \tag{A.2}$$

The minimum velocity of ion in the electrostatic potential ϕ is calculated from the slowest ion starting from rest and the ion accelerates to the velocity $v_{\min,i} = (-2e\phi/m_i)^{1/2}$. The minimum velocity of electron in the electrostatic potential ϕ is the electron that reach the zero velocity at the collector and travels back to the source with the velocity $v_{\min,e} = (-2/m_e)^{1/2}[e\phi - e\phi_C]^{1/2}$, where ϕ_C is the potential at the collector.

The particle density and flux are calculated by

$$n_\alpha(\phi) = \int_{v_{\min,\alpha}}^{\infty} f_\alpha(\phi, v) dv \tag{A.3}$$

$$\Gamma_\alpha(\phi) = \int_{v_{\min,\alpha}}^{\infty} v_x f_\alpha(\phi, v) dv \tag{A.4}$$

The flux of electron and ion become

$$\Gamma_e(\phi) = n_{e0} \left(\frac{kT_e}{2\pi m_e} \right)^{1/2} \exp\left(\frac{e\phi_C}{kT_e} \right) \tag{A.5}$$

$$\Gamma_i(\phi) = n_{i0} \left(\frac{kT_i}{2\pi m_i} \right)^{1/2} \tag{A.6}$$

Γ_e and Γ_i are constant in space. For the stable sheath formation, the current equal to zero at the collector, thus Eq. (A.5) equal to Eq. (A.6). This gives the ion to electron density ratio of the source as

$$\frac{n_{i0}}{n_{e0}} = \left(\frac{m_i}{m_e} \frac{T_e}{T_i} \right)^{1/2} \exp\left(\frac{e\phi_C}{kT_e} \right) \tag{A.7}$$

This equation can be used to calculate the collector sheath potential, ϕ_C. For the particle density, Eq. (A.3) gives

$$n_e(\phi) = \frac{n_{e0}}{2} \exp\left(\frac{e\phi}{kT_e} \right) \left[1 + \mathrm{erf}\left(\frac{e\phi - e\phi_C}{kT_e} \right)^{1/2} \right] \tag{A.8}$$

$$n_i(\phi) = \frac{n_{i0}}{2} \exp\left(-\frac{e\phi}{kT_i} \right) \mathrm{erfc}\left(-\frac{e\phi}{kT_i} \right)^{1/2} \tag{A.9}$$

The source potential drop ϕ_P must be satisfied by $\nabla^2 \phi_P = 0$. Thus, the charge density becomes zero or $n_e = n_i$. This gives

$$\begin{aligned} n_{e0} \exp\left(\frac{e\phi_P}{kT_e} \right) \left[1 + \mathrm{erf}\left(\frac{e\phi_P - e\phi_C}{kT_e} \right)^{1/2} \right] \\ = n_{i0} \exp\left(-\frac{e\phi_P}{kT_i} \right) \mathrm{erfc}\left(-\frac{e\phi_P}{kT_i} \right)^{1/2} \end{aligned} \tag{A.10}$$

Another relation for ϕ_P is that $\partial \phi_P / \partial x = 0$ or $E_x(\phi_P) = 0$. With Eq. (A.7) and Eq. (A.10), ϕ_c and ϕ_p are calculated and compared with the simulation results.

The simulation system is initially set with free of plasma and the particles are injected from the right hand side of the system, $x = L$ where L is the system length. The particles are fully absorbed at the divertor target at $x = 0$ at which the wall charge density σ is accumulated. The particle sources is half maxwellian

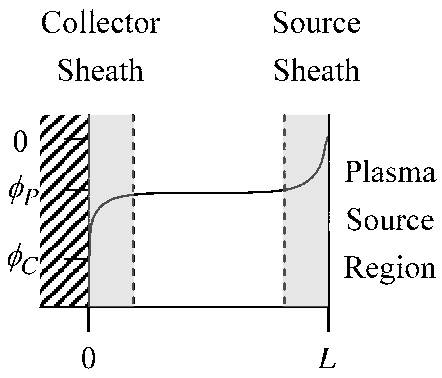

Figure A.1: Potential profile of the collector and source sheath. [71]

System length	$L = 0.03$ m
Mass ratio	$m_i/m_e = 1836$
Electron source temperature	$kT_{e0} = 1$ eV
Source particle density	$n_{e0} = n_{i0} = 5.6 \times 10^{13}\text{m}^{-3}$

Table A.1: Simulation Parameters

distribution where the current density of the ion and electron sources (j_{i0}, j_{e0}) are the initial input parameters. The current density is related to the source particle density, $j_{e0} = \sqrt{2/\pi}(qn_{e0}v_{Te0})$. The plasma density is set to be nearly the same as Q-machine, which has low plasma density. The overview of the system parameters are given in the table A.1. The unit of simulation results are based on SI unit.

The simulation is carried out with fixed electron source temperature, $kT_{e0} = 1$ eV. The ion source temperature, kT_{i0} is varied from 0.1 eV to 10 eV. The theoretical and simulation results are shown in Table A.2 and Fig.A.2. The simulation results are in agreement with the theory.

kT_i (eV)	Theory		Simulation	
	ϕ_C	ϕ_P	ϕ_C	ϕ_P
0.1	-4.90	no solution	-4.78	no solution
0.5	-4.10	-2.04	-4.16	-2.0
1	-3.75	-1.70	-3.47	-1.63
2	-3.41	-1.41	-3.40	-1.37
10	-2.60	-0.973	-2.59	-0.91

Table A.2: Simulation Parameters for $kT_{e0} = 1$ eV.

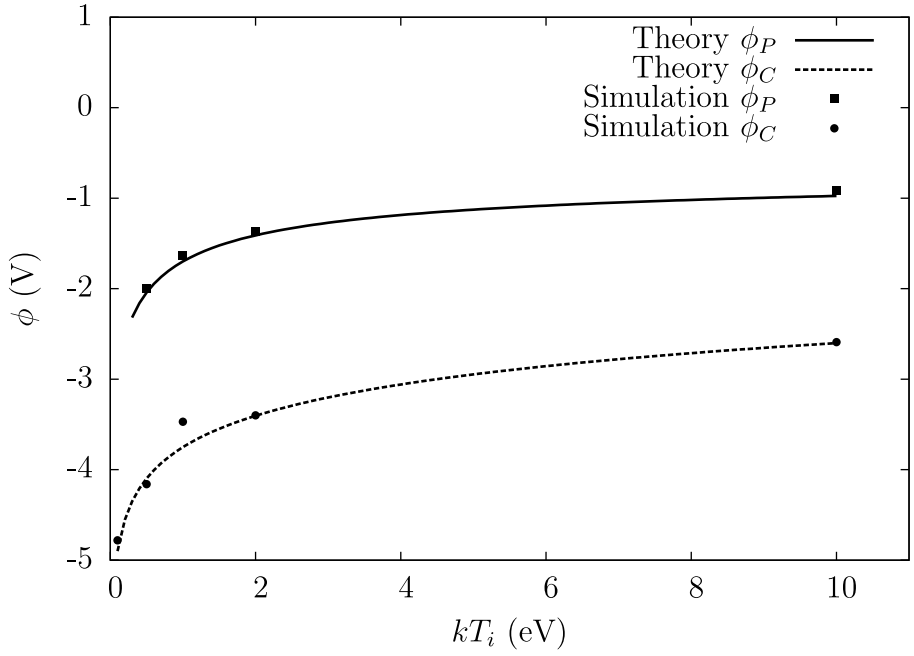

Figure A.2: ϕ_P and ϕ_C versus ion temperature.

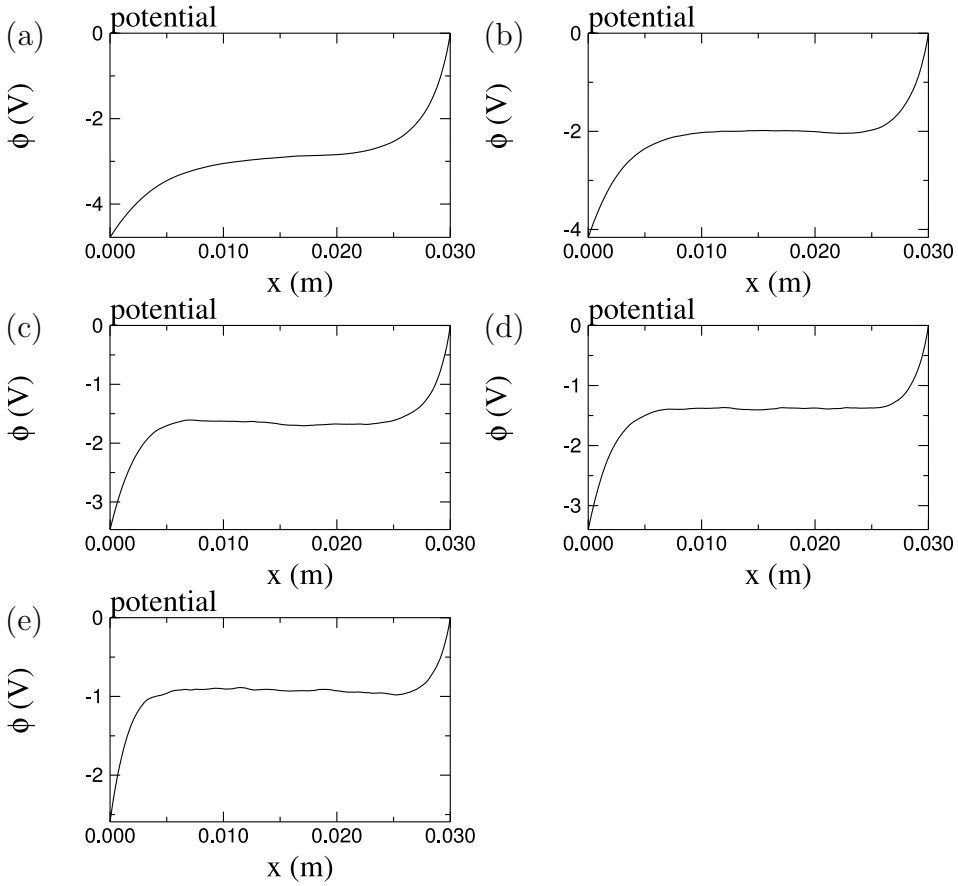

Figure A.3: Potential profile for (a) $kT_{i0} = 0.1$, (b) $kT_{i0} = 0.5$, (c) $kT_{i0} = 1$, (d) $kT_{i0} = 2$ and (e) $kT_{i0} = 10$.

Appendix B

Effects of Coulomb collision in PIC simulation

As mention in previous section, the PIC simulation alone does not properly treat the small angle collision within the Debye length. Here we apply the Nanbu model described in the preceding section to spatially uniform plasmas. The results of the Coulomb collision effect are obtained. The phenomena that will be tested are the relaxation of the anisotropic velocity distribution, the relaxation of the electron flow in the background ion and the equilibration of electron and ion temperature.

For the the relaxation of the anisotropic velocity distribution, we consider electron with $T_x \neq T_y = T_z$, where $T_x = 1.3T_y$. The normalized collision frequency is given as

$$\nu_0 = \frac{n_e e^4 \ln \Lambda}{8\pi\sqrt{2}\epsilon_0^2 m_e^{1/2} (kT_e)^{3/2}}.$$

Then the analytic solution becomes [55]

$$\Delta T = (\Delta T)_0 \exp\left(\frac{8}{5\sqrt{2}}\nu_0 t\right).$$

The number of particle in the simulation is 100,000. The results are shown in Fig. B.1 by changing the collision time step Δt_c. Both small and large collision time step gives a good agreement with the theoretical model.

Next, we show the results of the relaxation of the electron flow in the background ion. The initial condition is assumed with $T_0 = T_i = T_e$. The relaxation equation becomes

$$\frac{dV}{d(\nu_0 t)} = -\left(\frac{kT_0}{E_f}\right)^{3/2} \mu\left(\frac{E_f}{kT_e}\right) V,$$

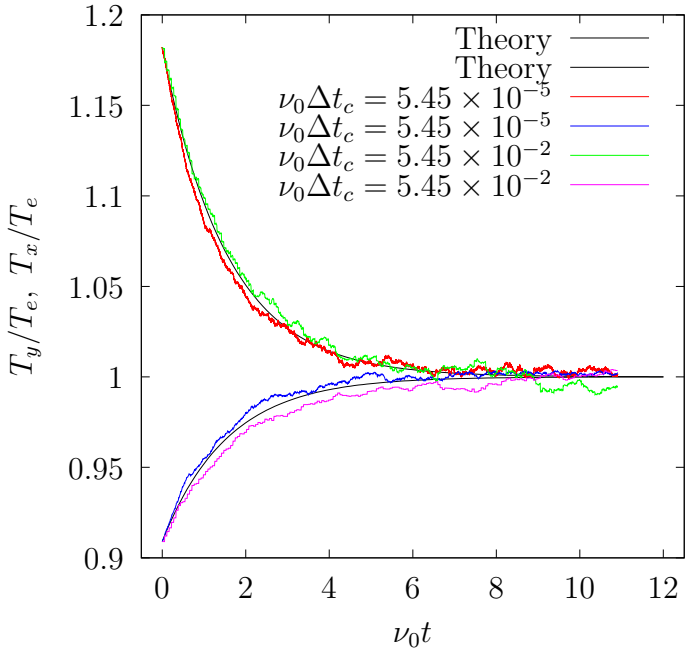

Figure B.1: Relaxation of temperature components.

where $\mu(x^2) = erf(x) - 2xe^{-x^2}/\sqrt{\pi}$. The real mass ratio for hydrogen plasma is used in our simulation. The simulation results are shown in Fig. B.2. The simulation does not agree in the later time because the analytic solution assume that electron distribution function is always in the Maxwellian, however the distribution function at the end of time step does not always be in the Maxwellian during the relaxation process.

The last case is the equilibration of electron and ion temperature. The relaxation equation is

$$d(T_i - T_e)/d(\nu_0 t) = -2\nu_{\rm eq}(T_i - T_e),$$

where

$$\nu_{\rm eq} = \frac{8}{3\pi^{1/2}}\frac{m_e}{m_i}\left(1 + \frac{m_e}{m_i}\frac{T_{i0}}{T_{e0}}\right)^{-3/2}.$$

The initial conditions are $m_i/m_e = 4$ and $T_{i0}/T_{e0} = 1/2$. The simulation results are shown in Fig. B.3.

These results give the Nanbu model as a good candidate for the treatment of the Coulomb collision in PIC simulation.

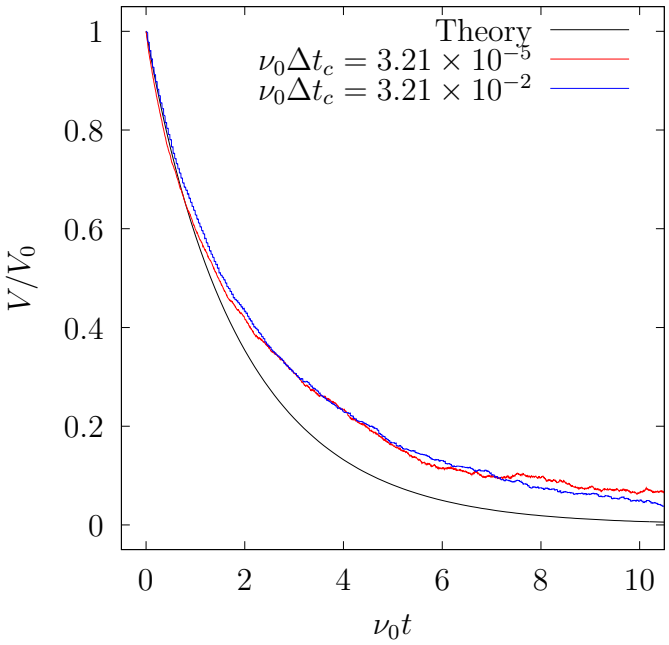

Figure B.2: Relaxation of flow velocity.

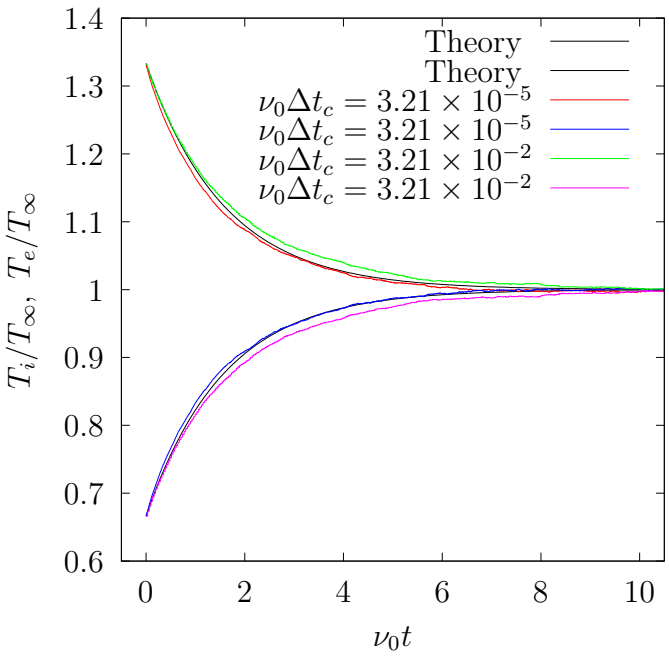

Figure B.3: Equilibration of electron and ion temperatures.

Acknowledgements

First of all, I would like to express my gratitude to Prof. Seiji Ishiguro for all of his advice to this research during my study. I appreciate every suggestions and discussion from him.

I also wish to extend my thanks to Dr. H. Hasegawa for the advice of simulation techniques and detailed knowledge about PIC simulation.

I owe special thanks to Dr. R. Kanno for his ideas on this work and Prof. A. Hatayama for his discussions, which motivate a lot to our research. I would like to thanks to Dr. T. Moritaga and Dr. S. Satake for providing support to improve my works.

My thanks also extend to Prof. R. Horiuchi, Dr. G. Kawamura, Dr. Y. Suzuki for all the comments on my study.

This work is supported by Monbukagakusho scholarship from the Japanese government.

References

[1] A. Loarte, B. Lipschultz, A.S. Kukushkin, G.F. Matthews, P.C. Stangeby, N. Asakura, G.F. Counsell, G. Federici, A. Kallenbach, K. Krieger, A. Mahdavi, V. Philipps, D. Reiter, J. Roth, J. Strachan, D. Whyte, R. Doerner, T. Eich, W. Fundamenski, A. Herrmann, M. Fenstermacher, P. Ghendrih, M. Groth, A. Kirschner, S. Konoshima, B. LaBombard, P. Lang, A.W. Leonard, P. Monier-Garbet, R. Neu, H. Pacher, B. Pegourie, R.A. Pitts, S. Takamura, J. Terry, E. Tsitrone, the ITPA Scrape-off Layer, and Divertor Physics Topical Group. Chapter 4: Power and particle control. *Nuclear Fusion*, 47(6):S203, 2007.

[2] G.F. Matthews. Plasma-surface interactions in controlled fusion devices plasma detachment from divertor targets and limiters. *Journal of Nuclear Materials*, 220:104 – 116, 1995.

[3] S. I. Krasheninnikov, A. S. Kukushkin, and A. A. Pshenov. Divertor plasma detachment. *Physics of Plasmas*, 23(5):055602, 2016.

[4] S.I. Krasheninnikov, M. Rensink, T.D. Rognlien, A.S. Kukushkin, J.A. Goetz, B. LaBombard, B. Lipschultz, J.L. Terry, and M. Umansky. Stability of the detachment front in a tokamak divertor. *Journal of Nuclear Materials*, 266269:251 – 257, 1999.

[5] N. Ohno, D. Nishijima, S. Takamura, Y. Uesugi, M. Motoyama, N. Hattori, H. Arakawa, N. Ezumi, S. Krasheninnikov, A. Pigarov, and U. Wenzel. Static and dynamic behaviour of plasma detachment in the divertor simulator experiment NAGDIS-II. *Nuclear Fusion*, 41(8):1055, 2001.

[6] W. L. Hsu, M. Yamada, and P. J. Barrett. Experimental simulation of the gaseous tokamak divertor. *Phys. Rev. Lett.*, 49:1001–1004, Oct 1982.

[7] N. Ohno, N. Ezumi, S. Takamura, S. I. Krasheninnikov, and A. Yu. Pigarov. Experimental evidence of molecular activated recombination in detached recombining plasmas. *Phys. Rev. Lett.*, 81:818–821, Jul 1998.

[8] T. Takizuka, K. Tani, M. Azumi, and K. Shimizu. Particle simulation of divertor plasma. *Journal of Nuclear Materials*, 128:104 – 110, 1984.

[9] R. J. Procassini and C. K. Birdsall. Particle simulation model of transport in a bounded, coulomb collisional plasma. *Physics of Fluids B: Plasma Physics*, 3(8):1876–1891, 1991.

[10] O. V. Batishchev, X. Q. Xu, J. A. Byers, R. H. Cohen, S. I. Krasheninnikov, T. D. Rognlien, and D. J. Sigmar. Kinetic effects on particle and heat fluxes in detached plasmas. *Physics of Plasmas*, 3(9):3386–3396, 1996.

[11] O. V. Batishchev, S. I. Krasheninnikov, Peter J. Catto, A. A. Batishcheva, D. J. Sigmar, X. Q. Xu, J. A. Byers, T. D. Rognlien, R. H. Cohen, M. M. Shoucri, and I. P. Shkarofskii. Kinetic effects in tokamak scrape-off layer plasmas. *Physics of Plasmas*, 4(5):1672–1680, 1997.

[12] A. Bergmann. Transport of edge-localized mode energy in a scrape-off layer in the presence of collisionless fast electrons. *Nuclear Fusion*, 42(9):1162, 2002.

[13] T. Shibata, J. Inamori, and A. Hatayama. Modeling of plasma and neutral interaction during {ELM} burst. *Journal of Nuclear Materials*, 415(1, Supplement):S873 – S876, 2011. Proceedings of the 19th International Conference on Plasma-Surface Interactions in Controlled Fusion.

[14] V. A. Abramov, Yu. L. Igitkhanov, V. I. Pistunovich, and V. A. Pozharov. First wall and divertor plate sputtering in a tokamak reactor. *Journal of Nuclear Materials*, 162:462 – 466, 1989.

[15] A. Kirschner, V. Philipps, J. Winter, and U. Kgler. Simulation of the plasma-wall interaction in a tokamak with the monte carlo code ero-textor. *Nuclear Fusion*, 40(5):989, 2000.

[16] S. E. Parker, R. J. Procassini, C. K. Birdsall, and B. I. Cohen. A suitable boundary condition for bounded plasma simulation without sheath resolution. *Journal of Computational Physics*, 104(1):41 – 49, 1993.

[17] J. Loizu, P. Ricci, and C. Theiler. Existence of subsonic plasma sheaths. *Phys. Rev. E*, 83:016406, Jan 2011.

[18] J. Loizu, P. Ricci, F. D. Halpern, and S. Jolliet. Boundary conditions for plasma fluid models at the magnetic presheath entrance. *Physics of Plasmas*, 19(12):122307, 2012.

[19] M. D. Campanell. Negative plasma potential relative to electron-emitting surfaces. *Phys. Rev. E*, 88:033103, Sep 2013.

[20] C. K. Birdsall and A. B. Langdon. *Plasma Physics via Computer Simulation*. Taylor & Francis Group, 2005.

[21] K. Nanbu. Probability theory of electron-molecule, ion-molecule, molecule-molecule, and coulomb collisions for particle modeling of materials processing plasmas and cases. *Plasma Science, IEEE Transactions on*, 28(3):971–990, Jun 2000.

[22] L. Spitzer and R. Härm. Transport phenomena in a completely ionized gas. *Phys. Rev.*, 89:977–981, Mar 1953.

[23] S.I. Braginskii. Transport Processes in a Plasma. *Reviews of Plasma Physics*, 1:205, 1965.

[24] P. C. Stangeby. *The plasma boundary of magnetic fusion devices*. Plasma physics series. Taylor & Francis, 2000.

[25] S. Nakazawa, N. Nakajima, M. Okamoto, and N. Ohyabu. One-dimensional simulation on stability of detached plasma in a tokamak divertor. *Plasma Physics and Controlled Fusion*, 42(4):401, 2000.

[26] M. Nakamura, Y. Ogawa, N. Shinji, R. Hiwatari, and K. Okano. multi-layer one-dimensional model for stability analysis on partially detached divertor plasmas. *Journal of Nuclear Materials*, 415(1):S553 – S556, 2011. Proceedings of the 19th International Conference on Plasma-Surface Interactions in Controlled Fusion.

[27] E. Zawaideh, F. Najmabadi, and R. W. Conn. Generalized fluid equations for parallel transport in collisional to weakly collisional plasmas. *The Physics of Fluids*, 29(2):463–474, 1986.

[28] Y. Shimomura, M. Keilhacker, K. Lackner, and H. Murmann. Characteristics of the divertor plasma in neutral-beam-heated asdex discharges. *Nuclear Fusion*, 23(7):869, 1983.

[29] G.M. McCracken, M.F. Stamp, R.D. Monk, A.G. Meigs, J. Lingertat, R. Prentice, A. Starling, R.J. Smith, and A. Tabasso. Evidence for volume recombination in jet detached divertor plasmas. *Nuclear Fusion*, 38(4):619, 1998.

[30] C. S. Pitcher and P. C. Stangeby. Experimental divertor physics. *Plasma Physics and Controlled Fusion*, 39(6):779, 1997.

[31] B. Lipschultz, J. Goetz, B. LaBombard, G.M. McCracken, J.L. Terry, M. Graf, R.S. Granetz, D. Jablonski, C. Kurz, A. Niemczewski, and J. Snipes. Dissipative divertor operation in the alcator c-mod tokamak. *Journal of Nuclear Materials*, 220:50 – 61, 1995. Plasma-Surface Interactions in Controlled Fusion Devices.

[32] R. Schneider, X. Bonnin, K. Borrass, D. P. Coster, H. Kastelewicz, D. Reiter, V. A. Rozhansky, and B. J. Braams. Plasma edge physics with b2-eirene. *Contributions to Plasma Physics*, 46(1-2):3–191, 2006.

[33] T. Takizuka, M. Hosokawa, and K. Shimizu. Particle simulation of detached plasma in the presence of diffusive particle loss and radiative energy loss. *Journal of Nuclear Materials*, 290(Supplement C):753 – 756, 2001.

[34] A. Froese, T. Takizuka, and M. Yagi. Electron parallel heat transport in the scrape-off layer using a particle-in-cell code. *Plasma and Fusion Research*, 5:S1017–S1017, 2010.

[35] D. Tskhakaya. On recent massively parallelized pic simulations of the sol. *Contributions to Plasma Physics*, 52(5-6):490–499, 2012.

[36] D. Tskhakaya and M. Groth. Modelling of tungsten re-deposition coefficient. *Journal of Nuclear Materials*, 463:624 – 628, 2015.

[37] D. Tskhakaya, K. Matyash, R. Schneider, and F. Taccogna. The particle-in-cell method. *Contributions to Plasma Physics*, 47(8-9):563–594, 2007.

[38] W. S. Lawson. Particle simulation of bounded 1d plasma systems. *Journal of Computational Physics*, 80(2):253 – 276, 1989.

[39] J.P. Verboncoeur, M.V. Alves, V. Vahedi, and C.K. Birdsall. Simultaneous potential and circuit solution for 1d bounded plasma particle simulation codes. *Journal of Computational Physics*, 104(2):321 – 328, 1993.

[40] G. A. Emmert, R. M. Wieland, A. T. Mense, and J. N. Davidson. Electric sheath and presheath in a collisionless, finite ion temperature plasma. *The Physics of Fluids*, 23(4):803–812, 1980.

[41] J. T. Scheuer and G. A. Emmert. A collisional model of the plasma presheath. *The Physics of Fluids*, 31(6):1748–1756, 1988.

[42] R. J. Procassini, C. K. Birdsall, and B.I. Cohen. Particle simulations of collisional transport in a high recycling, diverted tokamak scrape-off layer. *Nuclear Fusion*, 30(11):2329, 1990.

[43] K. Nanbu. Simple method to determine collisional event in monte carlo simulation of electron-molecule collision. *Japanese Journal of Applied Physics*, 33(8R):4752, 1994.

[44] V. Vahedi and M. Surendra. A monte carlo collision model for the particle-in-cell method: applications to argon and oxygen discharges. *Computer Physics Communications*, 87(1):179 – 198, 1995.

[45] R. K. Janev, D. Reiter, and U. Samm. *Collision processes in low-temperature hydrogen plasmas*, volume 4105 of *Berichte des Forschungszentrums Jülich*. Forschungszentrum, Zentralbibliothek, Jülich, 2003.

[46] D. R. Schultz, S. Y.. Ovchinnikov, and S. V. Passovets. *Elastic and Related Cross Sections for Low-Energy Collisions among Hydrogen and Helium Ions, Neutrals, and Isotopes*, pages 279–307. Springer US, Boston, MA, 1995.

[47] S. Trajmar and Isik Kanik. *Elastic and Excitation Electron Collisions with Atoms*, pages 31–58. Springer US, Boston, MA, 1995.

[48] C. B. Opal, W. K. Peterson, and E. C. Beaty. Measurements of secondary-electron spectra produced by electron impact ionization of a number of simple gases. *The Journal of Chemical Physics*, 55(8):4100–4106, 1971.

[49] M. Surendra, D. B. Graves, and G. M. Jellum. Self-consistent model of a direct-current glow discharge: Treatment of fast electrons. *Phys. Rev. A*, 41:1112–1125, 1990.

[50] C. K. Birdsall. Particle-in-cell charged-particle simulations, plus monte carlo collisions with neutral atoms, pic-mcc. *IEEE Transactions on Plasma Science*, 19(2):65–85, Apr 1991.

[51] R. J. Kanzleiter, D. P. Stotler, C. F. F. Karney, and D. Steiner. Improved elastic collision modeling in degas 2 for low-temperature plasmas. *Physics of Plasmas*, 7(12):5064–5069, 2000.

[52] A. B. Langdon and C. K. Birdsall. Theory of plasma simulation using finite-size particles. *The Physics of Fluids*, 13(8):2115–2122, 1970.

[53] H. Okuda and C. K. Birdsall. Collisions in a plasma of finitesize particles. *The Physics of Fluids*, 13(8):2123–2134, 1970.

[54] R. Shanny, J. M. Dawson, and J. M. Greene. Onedimensional model of a lorentz plasma. *The Physics of Fluids*, 10(6):1281–1287, 1967.

[55] T. Takizuka and H. Abe. A binary collision model for plasma simulation with a particle code. *Journal of Computational Physics*, 25(3):205 – 219, 1977.

[56] K. Nanbu. Theory of cumulative small-angle collisions in plasmas. *Phys. Rev. E*, 55:4642–4652, Apr 1997.

[57] A. V. Bobylev and K. Nanbu. Theory of collision algorithms for gases and plasmas based on the boltzmann equation and the landau-fokker-planck equation. *Phys. Rev. E*, 61:4576–4586, Apr 2000.

[58] C. Wang, T. Lin, R. Caflisch, B. I. Cohen, and A. M. Dimits. Particle simulation of coulomb collisions: Comparing the methods of takizuka & abe and nanbu. *Journal of Computational Physics*, 227(9):4308 – 4329, 2008.

[59] K. Nanbu and S. Yonemura. Weighted particles in coulomb collision simulations based on the theory of a cumulative scattering angle. *Journal of Computational Physics*, 145(2):639 – 654, 1998.

[60] H. Abe, J. Miyamoto, and R. Itatani. Grid effects on the plasma simulation by the finite-sized particle. *Journal of Computational Physics*, 19(2):134 – 149, 1975.

[61] E Kawamura, C K Birdsall, and V Vahedi. Physical and numerical methods of speeding up particle codes and paralleling as applied to rf discharges. *Plasma Sources Science and Technology*, 9(3):413, 2000.

[62] B. Di Martino, S. Briguglio, G. Vlad, and P. Sguazzero. Parallel pic plasma simulation through particle decomposition techniques. *Parallel Computing*, 27(3):295 – 314, 2001.

[63] E. Kawamura and C. K. Birdsall. Effect of coulomb scattering on low-pressure high-density electronegative discharges. *Phys. Rev. E*, 71:026403, Feb 2005.

[64] P. C. Liewer and V. K. Decyk. A general concurrent algorithm for plasma particle-in-cell simulation codes. *Journal of Computational Physics*, 85(2):302 – 322, 1989.

[65] R. D. Ferraro, P. C. Liewer, and V. K. Decyk. Dynamic load balancing for a 2d concurrent plasma pic code. *Journal of Computational Physics*, 109(2):329 – 341, 1993.

[66] N. Ezumi, S. Mori, N. Ohno, M. Takagi, S. Takamura, H. Suzuki, and J. Park. Density threshold for plasma detachment in gas target. *Journal of Nuclear Materials*, 241:349 – 352, 1997.

[67] S. I. Krasheninnikov, A. Yu. Pigarov, D. A. Knoll, B. LaBombard, B. Lipschultz, D. J. Sigmar, T. K. Soboleva, J. L. Terry, and F. Wising. Plasma recombination and molecular effects in tokamak divertors and divertor simulators. *Physics of Plasmas*, 4(5):1638–1646, 1997.

[68] K. Nanbu and K. Denpoh. Monte carlo collision simulation of positive-negative ion recombination for a given rate constant. *Journal of the Physical Society of Japan*, 67(4):1288–1290, 1998.

[69] D. Tskhakaya. Kinetic modelling of the plasma recombination. *Contributions to Plasma Physics*, 56(6-8):698–704, 2016.

[70] D. Stotler and C. Karney. Neutral gas transport modeling with degas 2. *Contributions to Plasma Physics*, 34(2-3):392–397, 1994.

[71] L. A. Schwager and C. K. Birdsall. Collector and source sheaths of a finite ion temperature plasma. *Physics of Fluids B: Plasma Physics (1989-1993)*, 2(5):1057–1068, 1990.

[72] R. C. Bissell and P. C. Johnson. The solution of the plasma equation in plane parallel geometry with a maxwellian source. *The Physics of Fluids*, 30(3):779–786, 1987.